Calculation of the Atomic Oxygen Fluence on the Van Allen Probes

G. Schumm[1], J.W. Bonnell[1], J.R. Wygant[2], F.S. Mozer[1,3]

[1]Space Sciences Laboratory, University of California, Berkeley, CA, USA
[2]School of Physics and Astronomy, University of Minnesota, Minneapolis, MN, USA
[3]Department of Physics, University of California, Berkeley, CA, USA

Key Points:

- The Van Allen Probes are exposed to high density atomic Oxygen close to perigee, that is known to degrade spacecraft surfaces.
- The atomic Oxygen fluence is modeled to explore the extent of degradation, when the most exposure occurred, and how it can be mitigated.
- The calculations can be replicated for past/future missions given their orbit parameters.

Abstract

The Van Allen Probes Mission consists of two identical spacecraft flying in highly elliptical orbits, with perigee altitudes originally near 600 km. During the low altitude periods of the orbits, the spacecrafts are immersed in a region of high-density atomic Oxygen. Atomic Oxygen is known to change and degrade the properties of spacecraft surfaces(Banks et al., 2004), such as those of the Van Allen Probes Electric Field and Waves (EFW) instrument. The consistency of the sensor surfaces in EFW is important because the mechanisms used to ensure the collection of high quality electric field measurements requires that the photoemission properties of each sensor are uniform and stable. Oxidation or erosion of the sensor surfaces could limit the instrument's ability to balance the currents produced by both the plasma electrons and the controlled bias current applied to the sensors, and thus to properly operate the device.

We have modeled the atomic Oxygen exposure to the spacecraft to help determine the impact it has had on the sensors. We have calculated the fluence (time integrated flux) of atomic Oxygen particles that have collided with the spacecrafts over the entire course of the mission. We have also looked at the distribution of atomic Oxygen flux over time to further analyze malfunctions in the sensor readings at different points along the course of the mission. Additionally, we have investigated how different surfaces of the spacecraft are affected differently due to their orientation with respect to the spacecraft's motion.

1 Introduction

The Van Allen Probes houses five instrument suites used to measure different properties and behaviors of Earth's radiation belts. The EFW suite utilizes three orthogonal sets of double-probe sensors, much like the electric field measurement devices used on previous missions, such as CRESS (Wygant et al., 1992) and THEMIS (Bonnell et al., 2008). Two of the six sensors lie along the spin-axis of the spacecraft, which rotates at approximately 5.5 RPM and points nearly towards the Sun (within 15° to 27°). The other four sensors lie within the spin-plane of the spacecraft which places them roughly in the y-z GSE plane (Wygant et al., 2013). The two spin-axis sensors are supported by 6-meter-long rigid booms rigid, whereas the spin-plane sensors are suspended by 50-meter-long, thin wire booms, which are kept taut by the centrifugal force imparted by the spacecrafts' rotation. An image of this set up in shown in Figure 1. The orientation of the spin-plane axis with respect to the Sun is important, as it is necessary that all spin-plane sensors are exposed to equal amount of solar illumination. The illumination of the spacecraft and its sensors will be discussed in depth later.

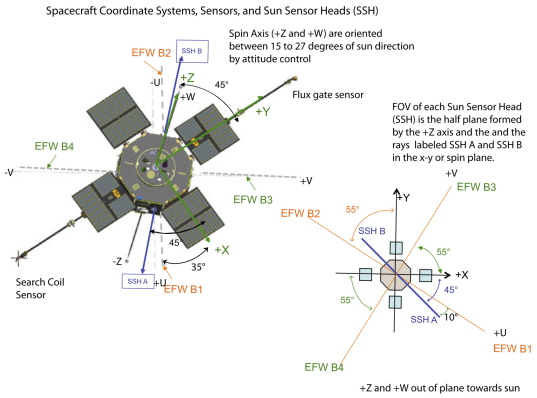

Figure 1: Overview picture of Van Allen Probes showing orientation of EFW spin-plane boom sensors and EFW axial boom sensors (Wygant et al., 2013).

The spacecraft is in an elliptical orbit with a perigee altitude of roughly 600 km and an apogee altitude of roughly 30,000 km (∼4.7 Earth radii), diagramed in the top image of Figure 2. This orbit does not stay fixed with respect to the Earth, but instead precesses, shown in the bottom image in Figure 2. Within the first year of the mission, the orbit apogee passed through all local Solar times due to this precession, which allows the

spacecraft to thoroughly sample Earth's radiation belts. However, this precession also has consequences on the spacecraft's atmospheric exposure.

The low perigee altitude immerses the spacecraft in a high-density atomic Oxygen regime for a portion of each orbit, which poses potential issues for the operation of the EFW instrument. The six Langmuir probes on the instrument consist of Aluminum spheres coated in DAG-213, an epoxy resin and graphite coating used to ensure there are minimal work function variations over the surface of the spheres (Wygant et al., 2013). Exposing DAG-213 to high density Oxygen plasma has been shown to directly inhibit the material's photoemission capabilities; the oxidized surfaces produce photoelectrons at a reduced rate (Samaniego et al., 2019). Quantifying the oxygen exposure to the spacecraft will help determine whether the instrument's measurement quality was compromised over the course of the mission.

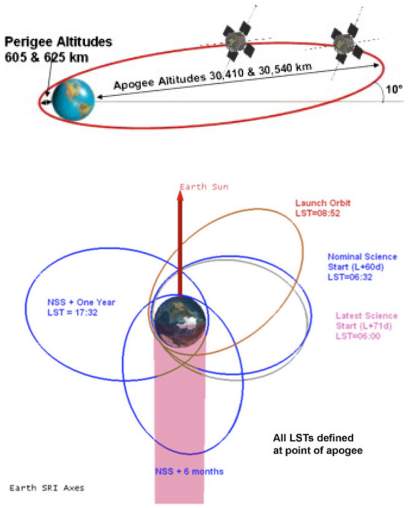

Figure 2: Diagram of Van Allen Probes orbit with orbit parameters (Srinivasan et al., 2012) (above) and diagram of orbital precession over the course of the mission (below) (Stratton et al., 2012) .

This paper will walk through the calculations of the atomic Oxygen flux and fluence for the orbit of the Van Allen Probes. The calculation uses the spacecraft flight coordinates from September 2012 to July 2019. However, the methods outlined can be generalized to any orbit, regardless of eccentricity, apogee altitude, or perigee altitude. The steps described include calculating atomic Oxygen density and the spacecraft velocity along the given orbital flight path, determining the flux contribution due to the thermal velocity of the atomic Oxygen molecules, factoring in the co-rotational velocity of Earth's atmosphere, and integrating the flux over time to produce the fluence of atomic Oxygen ions.

2 Methods

The flux and fluence calculations were developed using the methods derived by Bourassa and Gillis (1992) and the European Space Agency's Space Environment Information System (SPENIVS, 2018) . The following sections walk through these methods and outline how they are applied to the Van Allen Probes Mission.

2.1 Atomic Oxygen Density Calculation

The density of atomic Oxygen at any point along the spacecraft's trajectory is calculated using the US Naval Research Laboratory developed Mass Spectrometer and Incoherent Scatter Radar (NRLMSISE-00) Neutral Atmosphere model (Picone et al., 2002). This model provides the densities of Earth's atmosphere constituents at specified locations and times given the solar activity and space weather that day (F10.7 cm radio flux and Ap index value). The model also provides the temperature of the atmosphere at the specified locations and times. It is accurate from Earth's ground to an altitude of around 1000-km, encapsulating the range of altitudes near the spacecraft perigees.

2.2 Velocity Calculation

The flux of atomic Oxygen particles hitting the surface of a spacecraft is approximated as the density of particles at the spacecraft's location multiplied by the average speed

at which the particles collide with the spacecraft's surface at that location, termed the "ram velocity." The ram velocity of the particles is comprised of four main components: the spacecraft's velocity, the atmosphere's co-rotational velocity, the wind velocity, and the thermal motion of the atomic Oxygen particles.

$$\vec{v}_{ram} = -\vec{v}_{sc} + \vec{v}_{co} + \vec{v}_{wind} + \vec{u} \tag{1}$$

In addition, the rotational motion about the spacecraft's spin-axis is taken into consideration, $\vec{v}_{rot}$.

2.2.1 Spacecraft Velocity

As the speed at which the spacecraft is travelling increases, so does the number of particles that collide with its surface per unit time. These collisions become more frequent because the spacecraft occupies a larger volume of plasma in a given length of time as its speed increases. The ram velocity component attributed this motion is given by the negative of the spacecraft's velocity; if the spacecraft hits a particle with a velocity $\vec{v}$, it is equivalent to the particle hitting the spacecraft with a speed $-\vec{v}$. For the Van Allen Probes, the average magnitude of the spacecraft's velocity near perigee is around 9 km/s.

2.2.2 Co-rotational Velocity

Earth's atmosphere rotates along its spin-axis with the same angular frequency of the planet. The tangential velocity vector of the atmosphere at the position of the spacecraft is given by the cross-product of Earth's spin vector and the spacecraft's position vector:

$$\vec{v}_{co} = \vec{\omega} \times \vec{r}_{sc} \tag{2}$$

In a geocentric coordinate system, such as geocentric Earth inertial (GEI), the spin vector and position vector are defined as:

$$\vec{\omega} = \begin{bmatrix} 0 \\ 0 \\ \omega_{Earth} \end{bmatrix} \quad \& \quad \vec{r}_{sc} = \begin{bmatrix} r_{sc,x} \\ r_{sc,y} \\ r_{sc,z} \end{bmatrix} \tag{3}$$

Where $\omega_{Earth} = 7.293 \times 10^{-5}$ rad/s. Near the perigee of the Van Allen Probes, the magnitude of the atmosphere's co-rotational velocity is around 0.6 km/s.

2.2.3 Wind Velocity

The atomic Oxygen atoms have an additional velocity contribution from winds that exist in Earth's rotating atmosphere. The wind speeds in Earth's atmosphere are calculated using the Horizontal Wind Model 1993 (HWM93), an empirical model describing the velocity of the winds in the upper thermosphere (Hedin et al., 1996). The velocities are provided as zonal (West to East direction) and meridional (North to South direction) components given in an Earth-fixed frame. It is assumed that the wind has no radial (i.e. vertical) component.

This contribution can be written as a three-component vector in GEI coordinates, after a coordinate transformation, and added to the ram velocity vector in a similar manner to the co-rotational velocity vector. However, the magnitude of the wind velocity is small in comparison to the other velocities in play (on the order of 0.1 km/s), and thus only a marginally affects the magnitude of atomic Oxygen flux.

2.2.4 Thermal Velocity

The energy, and thus velocity, distribution of the atomic Oxygen ions in Earth's plasmasphere are described by the 3-D Maxwell-Boltzmann distribution:

$$f(\vec{u})du = \left(\frac{M}{2\pi RT}\right)^{\frac{3}{2}} e^{-\frac{M\vec{u}^2}{2RT}} d\vec{u} \tag{4}$$

Where M is the atomic mass of the ion in kg/kmol, R is ideal gas constant in J/K·kmol, T is the ambient temperature in K, and $\vec{u}$ is thermal velocity vector of the ions in m/s.

This equation describes the probability of finding a 3-dimensional particle with a velocity vector near $\vec{u}$, given the molecular mass and temperature of the gas its part of. At around 1,000 K (the temperature of the thermosphere near the spacecraft's perigee) the average thermal speed of an atom of atomic Oxygen is comparable to the spacecraft's velocity, given by:

$$\langle u \rangle = \sqrt{\frac{8RT}{M\pi}} \approx 1 \text{ km/s} \tag{5}$$

2.2.5 Average Incident Ram Velocity

Considering these four velocity components, we can now calculate the average incident ram velocity of the atomic Oxygen atoms striking a given surface of the spacecraft. The spacecraft velocity, co-rotational velocity, and wind velocity introduce a drift velocity to the atomic Oxygen gas in the reference frame of the spacecraft. The modified distribution function for the atomic Oxygen ram velocity is:

$$f(\vec{v}_{ram})du = \left(\frac{M}{2\pi RT}\right)^{\frac{3}{2}} e^{-\frac{M(\vec{v}_{ram}-\vec{v}_0)^2}{2RT}} d\vec{v}_{ram} \tag{6}$$

Where $\vec{v}_0 = -\vec{v}_{sc}+\vec{v}_{co}+\vec{v}_{wind}$. This modified equation gives the probability of finding an atomic Oxygen atom with a given *ram velocity*, rather than a given *thermal velocity*.

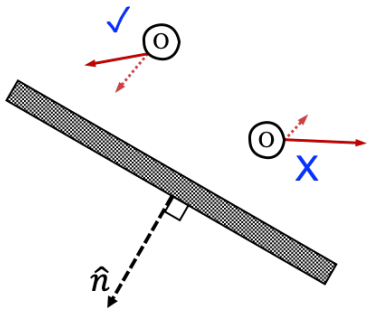

Figure 3: Example of surface and the corresponding normal vector, showing atomic Oxygen molecules with velocities that would and wouldn't result in collisions.

For a surface defined by the normal vector $\hat{n}$, as in Figure 3, the average velocity is calculated using the integral:

$$\langle v_{ram} \rangle = \iiint\limits_{(\vec{v}_{ram}\cdot\hat{n})>0} dv_{ram,x} \cdot dv_{ram,y} \cdot dv_{ram,z} \cdot (\vec{v}_{ram} \cdot \hat{n})\, f(\vec{v}_{ram}) \tag{7}$$

The distribution function is multiplied by the component of velocity normal to the chosen surface, and the bounds of integration are chosen so all particle velocities that would result in a collision are accounted for. In this case, the velocity component along the direction of the surface normal must be greater than zero for a collision to occur, demonstrated in Figure 3. The solid red arrows represent the two example particles' velocities, and the dotted red arrows denote their normal velocities.

This integral is simplified using the substitution $\vec{u} = \vec{v}_{ram} - \vec{v}_0$:

$$\langle v_{ram} \rangle = \iiint\limits_{(\vec{u}+\vec{v}_0)\cdot\hat{n}>0} du_x \cdot du_y \cdot du_z \left((\vec{u} + \vec{v}_0) \cdot \hat{n} \right) f(\vec{u}) \tag{8}$$

and further simplified using the coordinate transformation shown in Figure 4.

By rotating the coordinate system to one where the normal to the surface, $\hat{n}\,'$, lies along the x-axis, the dot products reduce to the x-components of the velocities in this new coordinate system. This transformation also simplifies the integral bounds, changing this from a 3-D problem to a 1-D problem. The integral in the transformed coordinate system (denoted by a prime) is:

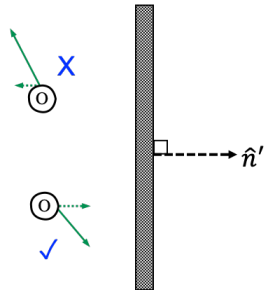

Figure 4: Example of surface after coordinate transformation.

$$\langle v_{ram} \rangle = \iiint\limits_{\left(\vec{u}\,'+\vec{v}_0'\right)_x>0} du'_x \cdot du'_y \cdot du'_z \left(\left(\vec{u}\,' + \vec{v}_0'\right)_x \right) f(\vec{u}\,') \tag{9}$$

With the full bounds of integration, we have:

$$\langle v_{ram} \rangle = \left(\frac{M}{2\pi RT} \right)^{\frac{3}{2}} \int_{-\infty}^{\infty} e^{-\frac{Mu_y'^2}{2RT}} du'_y \int_{-\infty}^{\infty} e^{-\frac{Mu_z'^2}{2RT}} du'_z \int_{-v'_{0,x}}^{\infty} \left(u'_x + v'_{0,x} \right) e^{-\frac{Mu_x'^2}{2RT}} du'_x \tag{10}$$

The solution simplifies to the closed-form equation:

$$\langle v_{ram} \rangle = \frac{1}{4} \langle u \rangle \left[s\sqrt{\pi} \left(\mathrm{erf}(s) + 1 \right) + e^{-s^2} \right] \tag{11}$$

$$\langle u \rangle = \sqrt{\frac{8RT}{M\pi}} \quad \& \quad s = \sqrt{\frac{M}{2RT}} v'_{0,x} = \frac{2}{\sqrt{\pi}} \frac{v'_{0,x}}{\langle u \rangle} \tag{12}$$

The speed $\langle u \rangle$ is the average thermal speed at a given temperature and particle mass, given by:

$$\langle u \rangle = \iiint \vec{u} f(\vec{u}) d\vec{u} \tag{13}$$

The variable s is a dimensionless parameter relating the magnitude of the normal component of the drift velocity to the average thermal speed of the particles. The error function, erf(), is defined as (Weisstein, 2020):

$$\mathrm{erf}(x) = \frac{2}{\sqrt{\pi}} \int_0^x e^{-t^2} dt \tag{14}$$

2.2.6 Rotational Velocity

The final component of velocity that is considered in the flux calculation is the rotational velocity of the spinning probes. The spacecraft spins along the axis of two of its sensors

(senors 5 & 6) at a rate of 5.5 ± 0.25 RPM (Wygant et al., 2013). The two sets of sensors in the spin-plane extend 50 meters from the spacecraft body, giving them a rotational velocity of:

$$v_{rot} = l \cdot \omega = (50 \text{ m}) \cdot (5.5 \text{ RPM} \times \frac{2\pi \text{ rad}}{60 \text{ s}}) = 28.8 \text{ m/s}$$

The flux corresponding to this motion is substantially smaller in magnitude than the flux contributions discussed above. However, the rotation of the spacecraft should still considered because it results in all four spin plane booms being exposed to the same amount of atomic Oxygen, regardless of the spacecraft orientation or motion (i.e. no sensors will be preferentially shielded by the spacecraft body).

2.3 Flux Calculation

2.3.1 Closed-form Equation for Flux

The flux across a surface that is not aligned with the spin-axis and defined by the normal vector $\hat{n}$ is given by the equation:

$$\Gamma = n_{AO} \left(\langle v_{ram} \rangle + v_{rot} \right) = \frac{1}{4} n_{AO} \langle u \rangle \left[s\sqrt{\pi} \left(\text{erf}(s) + 1 \right) + e^{-s^2} \right] + n_{AO} v_{rot} \tag{15}$$

We can look at the result of this equation for some limiting cases to verify its validity. In the case that the atomic Oxygen particles have no drift velocity and the spacecraft is not rotating, collisions with the spacecraft will be solely caused by the particles' thermal motion:

$$v_0 = v_{rot} = 0 \Rightarrow s \to 0 \Rightarrow \Gamma = \frac{1}{4} n_{AO} \langle u \rangle$$

This is the known result for collisions by ideal gas molecules with a stationary plane surface (Graham, 2007). We can also look at the limit where temperature goes to zero, resulting in no thermal motion:

$$\langle u \rangle = 0 \Rightarrow s \to \infty \Rightarrow \Gamma = n_{AO} v'_{0,x} + n_{AO} v_{rot}$$

In this case, the collisions with the spacecraft are caused solely by drift velocity of the particles in the direction normal to the surface, $v'_{0,x}$ and the rotation of the spacecraft. No thermal motion means that only particles moving towards the surface will result in collisions, which is why the x-component of the velocity in the prime coordinates is picked out (see Figure 4).

The last limiting case we can investigate is if the particles are moving away from the surface with great speed ($v'_{0,x} << 0$). In this scenario, we would expect no flux of atomic Oxygen atoms other than the small contribution from the rotation of the spacecraft, which doesn't depend on the direction of the particles' motion.

$$v'_{0,x} \to -\infty \Rightarrow s \to -\infty \Rightarrow \Gamma = n_{AO} v_{rot}$$

2.3.2 Flux Calculation Procedure

The process of calculating the flux of atomic Oxygen particles a single point along the spacecraft's orbit is as follows:

1. Load the spacecraft position data:
   - Load the position data in Geographic coordinates (GEO). This coordinate system in non-inertial, with the x-axis pointing towards the prime meridian (0 longitude), which rotates with Earth. The z-axis points along Earth's spin-axis and

the y-axis is perpendicular to both axes, lying in the equatorial plane. The position data, given in cartesian coordinates, is converted to the geographic spherical coordinates latitude, longitude, and altitude.

- Load the position data in Geocentric Earth Inertial coordinates (GEI). This inertial coordinate system does not rotate with the Earth. It shares the same z-axis as the GEO coordinate system, but has its x-axis pointing toward the Vernal Equinox, a direction that is practically constant with respect to the distant stars.

2. Load the spacecraft velocity data in GEI coordinates.
3. Load the spacecraft spin-axis vector data in GEI coordinates. This is later used to define the top and bottom of the spacecraft.
4. Prune the data to include only the position and velocity of the spacecraft ten minutes before and ten minutes after it has reached perigee for each orbit it completes. A twenty minute time range was chosen because it resulted in a negligible difference in the atomic Oxygen fluence for each orbit. This is explained by the exponential dependence on altitude of the neutral gas density as well as the $1/r$ dependence of the spacecraft orbital velocity (Banks et al., 2004). Figure 5 illustrates this phenomenon, as the atomic Oxygen density drops to nearly 0 ions/cm^3 at the beginning and end of the twenty minute time range.
5. Calculate the co-rotational atmosphere velocity using the spacecraft position in GEI coordinates, as described in section 2.2.2
6. Calculate the zonal and meridional wind velocities using the spacecraft position in GEO coordinates, as described in section 2.2.3. The wind velocities are converted to a vector in GEI coordinates by first treating the zonal direction as longitudinal (azimuthal) and the meridional direction as latitudinal (polar). The vector is then represented in GEO cartesian coordinates and transformed by a rotation matrix to GEI cartesian coordinates (Hapgood, 1992).

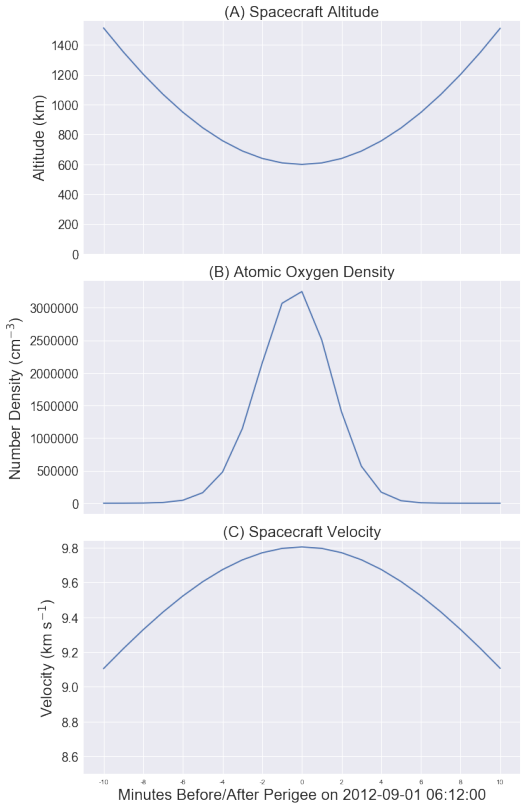

Figure 5: Plot of the spacecraft altitude (A), the atomic Oxygen density at the location of the spacecraft (B), and the spacecraft velocity (C) during a 20-minute window centered around perigee on September 1st, 2012 06:12 UTC.

7. Define the normal to the impact surface of interest. Some examples of normal vectors are:

   - The spin-axis of the spacecraft, provided by the direction of the spin angular momentum vector in GEI coordinates. This normal corresponds to the top or bottom of the spacecraft.
   - The atomic Oxygen drift velocity vector. This vector does not correspond to a specific surface because the spacecraft's orientation with respect to atomic Oxygen drift changes throughout orbit. However, this normal gives an indication of the maximum possible flux experienced by any surface on the spacecraft.

8. Vectorially sum the drift velocity components (spacecraft velocity, co-rotation, and wind) and transform to a coordinate system in which the defined normal vector

is in the $\hat{x}$ direction. The appropriate rotation matrix is constructed using the Rodrigues Rotation Formula (Fuhrmann, 1984).

9. Calculate the atomic Oxygen density and atmosphere temperature using the NRLMSIS-00 model discussed in section 2.1. The spacecraft position in GEO coordinates and the space weather at the given date, downloaded from the National Oceanic and Atmospheric Administration's Space Weather Enthusiasts Dashboard website (NOAA, 2020), are fed to the model.
10. Using the drift velocity, the ambient temperature, and the atomic Oxygen density, calculate the flux using equation 15.

2.4 Fluence Calculation

The flux calculation process is repeated for every point along the pruned spacecraft trajectory. The fluence, defined as the time integral of the flux over the course of the mission, is calculated using the trapezoid method of numerical integration. This is achieved with the summation:

$$\mathcal{F} = \int_{t_0}^{t_f} \Gamma(t) dt \approx \sum_{i=1}^{N} \frac{1}{2} \left(\Gamma_{i-1} + \Gamma_i\right) \Delta t \tag{16}$$

Where Δt is the length of time between the data points and N is the total number of data points.

3 Analysis

This procedure has been implemented for both Van Allen Probes (RBSP-A and RBSP-B) over the course of the mission (September 1st, 2012 to July 1st, 2019). Two surfaces/methods of defining a surface were considered:

1. A "worst/best case scenario" surface with a normal vector always parallel/antiparallel to the atomic Oxygen drift velocity.
2. The top and bottom surfaces of the spacecraft, defined by its spin angular momentum vector.

I have also broken down features of the fluence accumulation over time for the spacecrafts, providing insight into ways of mitigating atomic Oxygen exposure.

3.1 Worst Case Scenario Atomic Oxygen Fluence

A surface with a normal that is parallel to the atomic Oxygen gas drift velocity (see Figure 3) will experience the greatest flux of atoms and thus the greatest accumulation of fluence. Although no such surface exists on the spacecraft, this calculation gives an upper bound for the magnitude of atomic Oxygen fluence experience by the Van Allen Probes.

Figure 6 (top) shows shows the fluence accumulation for this surface over the course of the mission for both spacecrafts. The steep increase in fluence in 2019 is due to the perigee lowering maneuvers initiated at the end of the mission. At lower altitudes, the atomic Oxygen density, as well as the speed of the spacecraft, increase dramatically, resulting in a much higher flux of atomic Oxygen particles. Plots of the altitude and atomic Oxygen density at the perigees of each orbit are shown in Figure 6 (bottom), displaying this change.

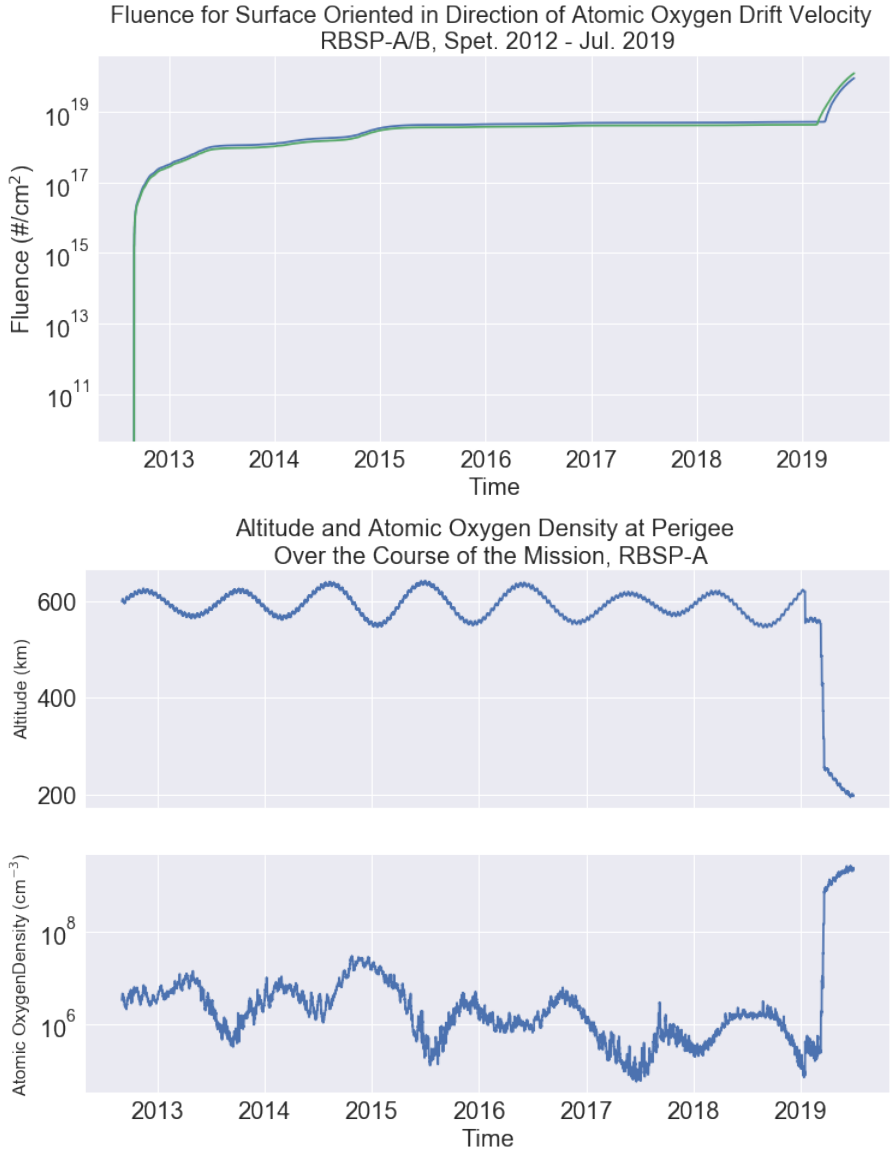

Figure 6: Fluence accumulation over the course of the mission (top), perigee altitude and atomic Oxygen density over the course of the mission (bottom)

To better analyze the features and trends present in the spacecraft's accumulation of fluence, Figure 7 shows the accumulated fluence on a linear scale, both before (top) and after (bottom) December of 2019. This removes the effects of the perigee lowering maneuvers on the fluence accumulation, and depicts how drastic an effect the lowered perigee has on the spacecraft's atomic Oxygen exposure. In addition, figure 7 (top) provides a more accurate description of the atomic Oxygen flux/fluence conditions over the course of the mission.

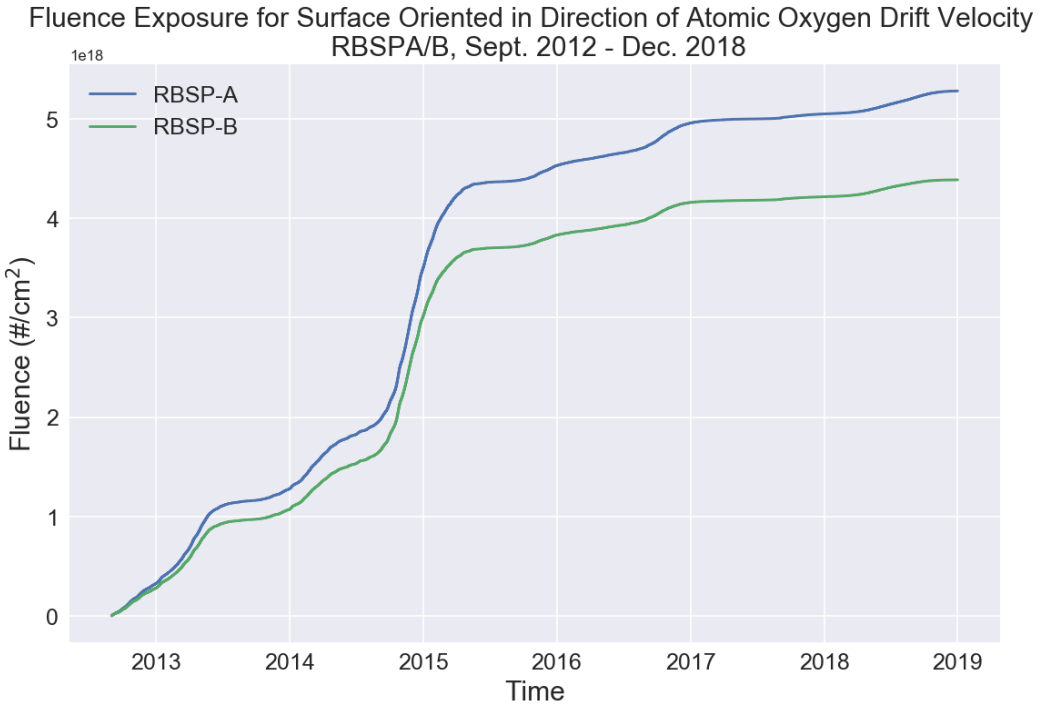

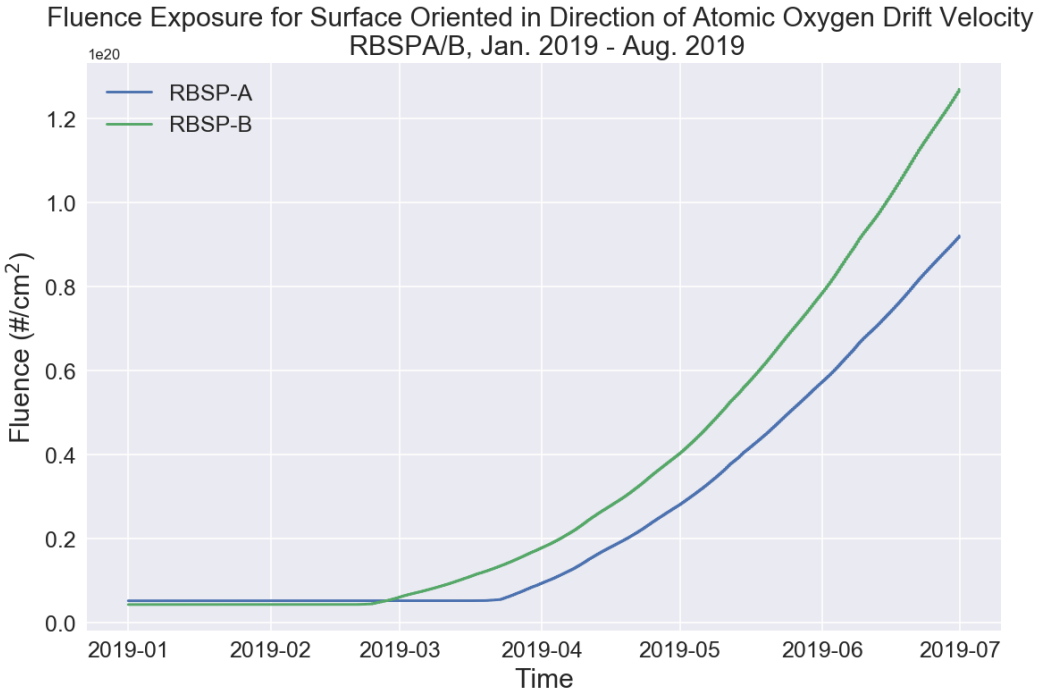

Figure 7: Fluence accumulation before (top) and after (bottom) December of 2019.

3.1.1 Increased Rate of Change of Fluence (i.e. Flux)

From 2012 to 2014, the fluence appears to increase with a relatively constant slope for both spacecrafts. However, from September 2014 to March 2015, the rate of change of fluence visibly spikes. Quantifying this trend for probe A, before September 2014, the fluence was increasing at an average rate of 2.78×10^{15} particles/cm^2 per day, whereas from September 2014 to March 2015, this rate increases to 1.11×10^{16} particles/cm^2 per day. The rate then decreased back down to 7.83×10^{14} particles/cm^2 per day from March 2015 to December 2018. The rate of fluence accumulation increases by a factor of ∼4 in the steeper region compared to the initial rate of increase, and by a factor of ∼14 compared to the final rate of increase(regions denoted by the dotted lines in Figure 8).

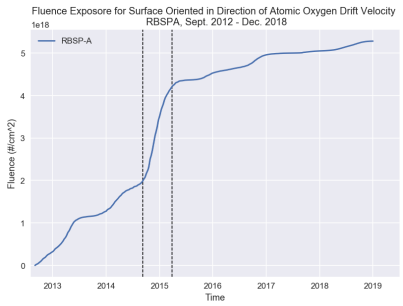

Figure 8: RBSP-A fluence accumulation showing regions of constant slope.

This trend can be explained by looking at the modeled atomic Oxygen density at perigee across the same time range. Figure 9 below shows the same altitude and density versus time plots in Figure 6 above, but in the shortened time range.

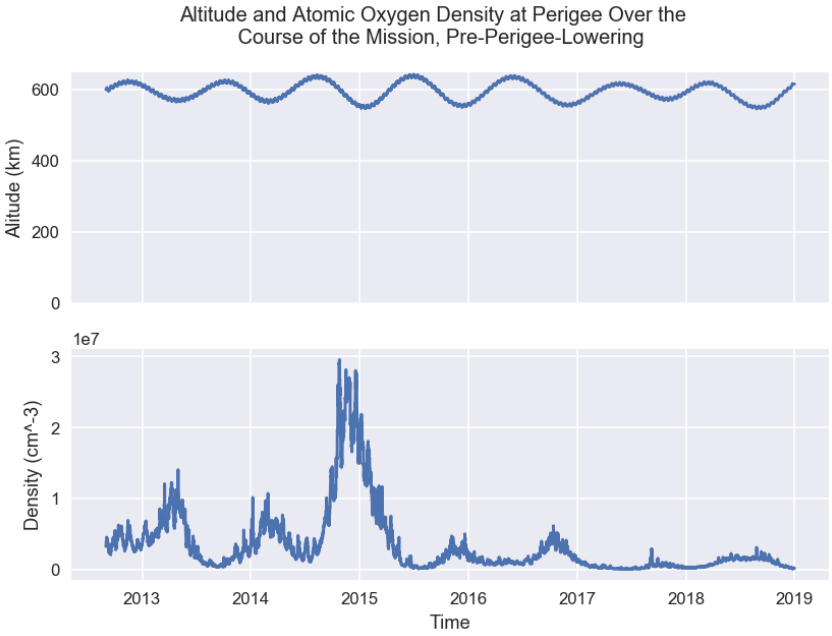

Figure 9: Perigee altitude and atomic Oxygen density before perigee lowering.

The spike in the density of atomic Oxygen at perigee aligns with the increased rate of change of fluence with no dramatic change in the perigee altitude (and thus spacecraft velocity). The flux of atomic Oxygen particles is directly related to the density, so the causal relationship between the increase and density and increase in fluence slope is justified. Figure 10 helps explain why this spike in density occurs.

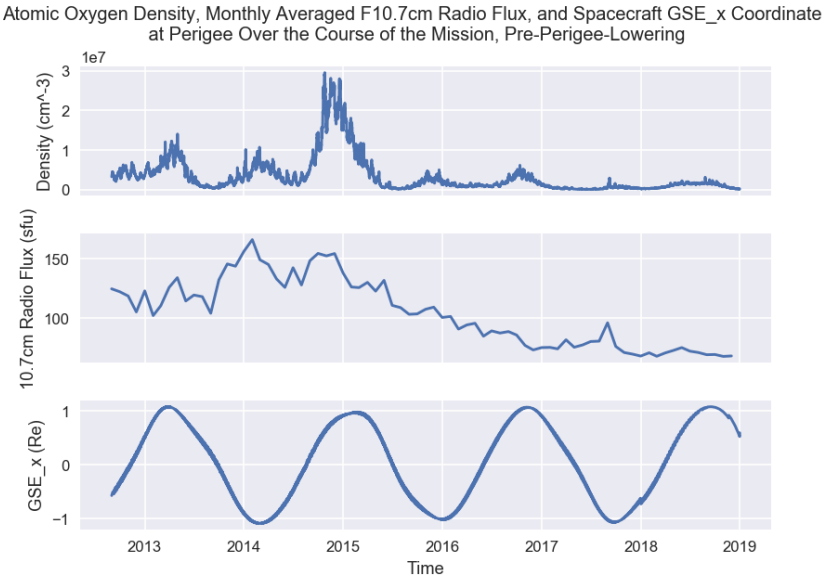

Figure 10: Atomic Oxygen density, F10.7cm radio flux value, and GSE-x coordinate of spacecraft at perigee, before perigee lowering.

The top plot in Figure 10 is the same atomic Oxygen density versus time graph as in Figure 9. The middle plot is the F10.7 cm radio flux value at the location and time of perigee, averaged over each month in the time range. The averaging was used to smooth out the otherwise noisy parameters that fluctuates about a base level throughout the month. The F10.7 cm radio flux is a strong indicator of solar activity, correlating with the number of Sunspots and level of UV irradiance from the Sun (Tapping, 2013). The higher this value, the more radiation from the Sun is reaching Earth's atmosphere and ionizing neutral O_2 molecules, producing atomic Oxygen.

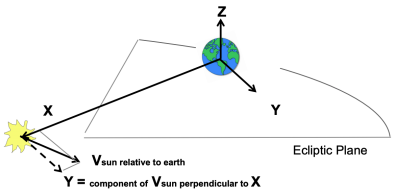

Figure 11: Diagram of Geocentric Solar Ecliptic (GSE) coordinate system (Acton, 1996).

The third plot is the x-coordinate of the spacecraft's position in Geocentric Solar Ecliptic (GSE) coordinates at the perigee of each orbit in units of Earth radii. In GSE coordinates, the origin is at the center of the Earth and the x-axis points towards the Sun, shown in Figure 11. When the x position of the spacecraft in this coordinate system is positive, the spacecraft lies between the Earth and the Sun. Conversely, when the x position of the spacecraft is negative, it lies behind Earth, shaded from the Sun.

The middle plot shows that there was an increase in solar activity from around mid 2013 to mid 2015. This is consistent with the Suns 11-year-periodic solar cycle, graphically shown in the plot in Figure 12 (Hathaway, 2015). Roughly every 11 years, the Sun's magnetic pole flips orientations. At the beginning and end of this 11-year cycle, the Sun's activity and the number of Sunspots are at minimums. At the midpoint of the cycle, the Sun's ac-

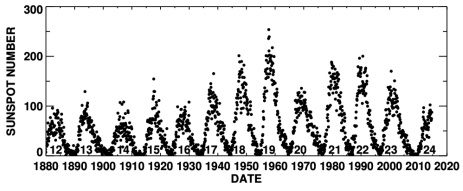

Figure 12: Number of Sunspots vs. time as an indicator of the Sun cycle (Hathaway, 2015).

tivity is at a maximum and the frequency of solar flares and coronal mass ejections is highest (Hathaway, 2015). This explains why the F10.7 cm radio flux was elevated from 2013 to 2015, the Sun was currently at its solar maximum.

The third plot explains why the atomic Oxygen density only spikes from September 2014 to March 2015, rather than over the course of the entire solar maximum. The spacecraft's orbit precesses around the Earth, changing its position at perigee with respect to the Earth-Sun line. When the GSE-x coordinate of the spacecraft at perigee is *positive*, the spacecraft is on the day side of the Earth whereas when GSE-x coordinate of the spacecraft at perigee is *negative*, the spacecraft is on the night side of the Earth. The elevated solar activity due to the Sun's solar maximum only affects the atomic Oxygen flux experienced by the spacecraft when it is on the day side of Earth, immersed in an atmosphere being bathed by solar radiation.

3.2 Best Case Scenario Atomic Oxygen Fluence

Similar to the worse case scenario, the best case scenario surface is one facing opposite to the atomic Oxygen gas drift velocity. This surface is being shielded from oncoming atomic Oxygen flux and should accumulate zero fluence from the drift velocity of the particles. The only collisions that occur are by atomic Oxygen atoms with random thermal motion so large that their trajectory strays from the drift velocity enough to direct their motion towards the surface. This should be an unlikely event, which is supported by the plot in Figure 13. The anti-parallel surface experiences a negligible amount of atomic Oxygen exposure compared to the parallel surface. The region where the anti-parallel surface does accumulate fluence is when the atomic Oxygen density is at its peak during the solar maximum. Otherwise, the the surface is nearly perfectly shielded.

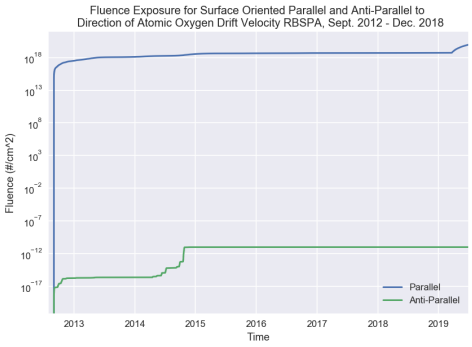

Figure 13: Comparison of fluence for surfaces alligned and anti-alligned to the atomic Oxygen drift velocity for RBSP-A.

Note that the graph in Figure 13 does not include the fluence contribution from the rotation of the spacecraft about its spin-axis.

3.3 Flux as a Function of Angle from Drift Velocity

The calculations for the best and worst case scenario spacecraft surfaces show that there is large variation in the flux as a function of the angle between the surface normal and the atomic Oxygen drift velocity. To investigate this relationship in more depth, the ram velocity as a function of both angle of incidence and the atomic Oxygen temperature was considered. Figure 15 shows the calculated atomic Oxygen ram velocity as a function of the approach angle at difference temperature. Equation 11 was used with the average atomic Oxygen drift velocity at perigee (~ 9.35 km/s) plugged in for the drift velocity term. Each curve is labeled with the ratio of the average thermal velocity of the gas at each temperature (from equation 12) to the drift velocity. For reference, the average temperature at perigee

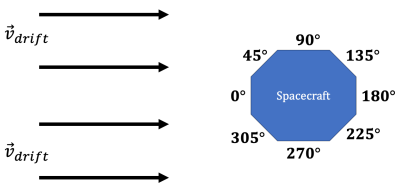

Figure 14: Diagram of spacecraft with surfaces labelled by their angle of incident to the atomic Oxygen drift velocity.

for the calculations in sections 3.1 and 3.2 corresponded to a velocity ratio of 0.124. The diagram in Figure 14 shows the spacecraft surfaces and their corresponding angle with respect to the atomic Oxygen gas. In the diagram, the spacecraft is moving leftwards through the gas, which is why the gas moves rightwards in the motionless spacecraft reference frame.

As discussed in the limiting case in section 2.3.1, when there is no thermal motion ($T = 0$ and $\langle u \rangle = 0$) the only collisions that occur are due to the parallel motion of the particles with respect to the surface normal of interest. This explains why the $\langle u \rangle / v_{drift} = 0$ curve falls to 0 m/s ram velocity from 90 degrees to 270 degrees; the normals of these surfaces are either perpendicular to the atomic Oxygen drift velocity or the surfaces are shielded from the atomic Oxygen drift. However, as the gas temperature increases, the thermal motion of the particles increases, allowing for the exposure of surfaces oriented away from the drift velocity. The affect becomes quite dramatic as the average thermal velocity surpasses the drift velocity.

For the Van Allen Probes, the temperature regime ($\langle u \rangle \approx 1$ km/s) is far from the extreme examples in Figure 16. However, even at this temperature, the effects are still felt by the side surfaces of the spacecraft.

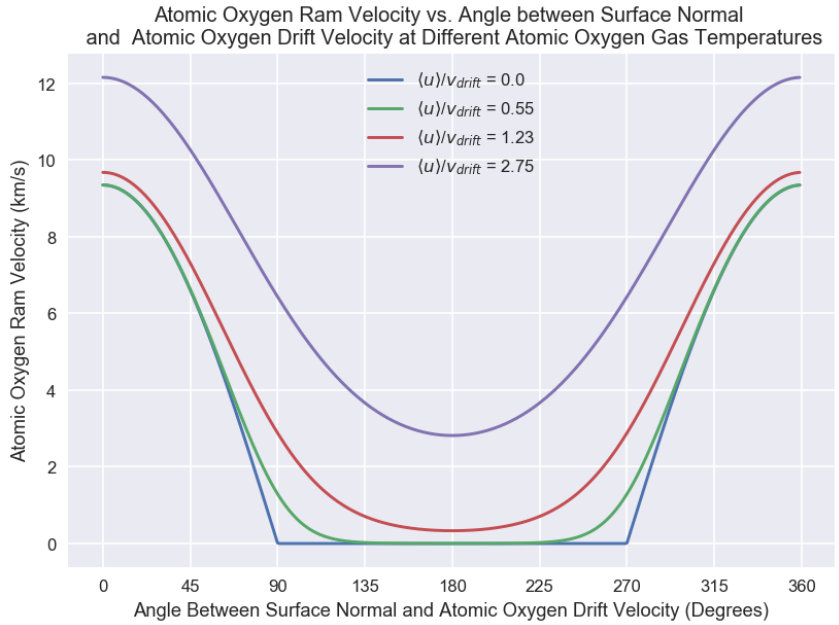

Figure 15: Plot of ram velocity vs. angle of incidence at different temperatures.

3.4 Top and Bottom Surfaces of Spacecraft (Sensors 5 & 6)

For the surfaces of the spacecraft that are in its spin-plane, such as EFW sensors 1, 2, 3, and 4, it is a difficult task to accurately calculate their incident atomic Oxygen flux. Considering the spin of the spacecraft, one must determine how to properly average the flux over each period of the spacecraft rotation. This task proves challenging given the varying time scales of the different contributions to the atomic Oxygen drift velocity. In addition, there shouldn't be any sensor-specific exposure; the rotation and orientation of the spacecraft should result in each spin-plane sensor being immersed in similar atomic Oxygen environments. However, this is not the case for the top and bottom surfaces of

the spacecraft. The spin-axis sensors will likely experience different intensities of atomic Oxygen exposure over the course of the mission due to the constant difference in their orientations. The surfaces parallel to the spin-axis of the spacecraft, ($\hat{L}$), be used as a proxy for determining the difference in the atomic Oxygen exposure between the top and bottom EFW sensors (5 and 6 respectively).

The angle between the spin-axis vector and the spacecraft velocity vector will play the largest role in the differences between the exposure to the top and bottom of the spacecraft. The diagram in Figure 16 displays this relationship. When $\vec{v}_{sc}$ is anti-aligned with $\hat{L}$ ($\hat{L} \cdot \vec{v}_{sc} < 0$, left image), the top surface is in the wake of the spacecraft, protected from atomic Oxygen exposure by the bottom surface and the spacecraft body. The converse is true for the opposite alignment, shown in the right image of Figure 16.

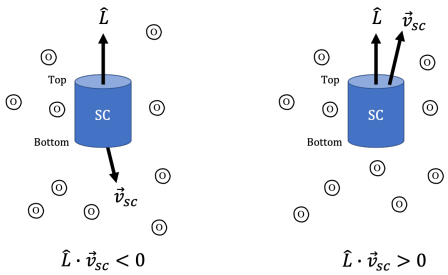

Figure 16: Diagram of spacecraft showing difference in atomic Oxygen exposure when velocity vector is aligned (right) vs. anti-aligned (left) to spin-axis vector.

As the Earth rotates around the Sun, the spacecraft's spin-axis is shifted to follow the movement of the Earth-Sun line. This causes the angle between the $\hat{L}$ and $\vec{v}_{sc}$ vectors near perigee to change over the course of the mission. While both the top and bottom surfaces should spend equal times in the wake of the spacecraft, we know that the atmospheric activity is not constant over the course of the mission (see section 3.1.1). Whichever surface is outside of the wake of the spacecraft during the solar maximum will experience a larger accumulation of fluence, which is shown in the plot in Figure 17.

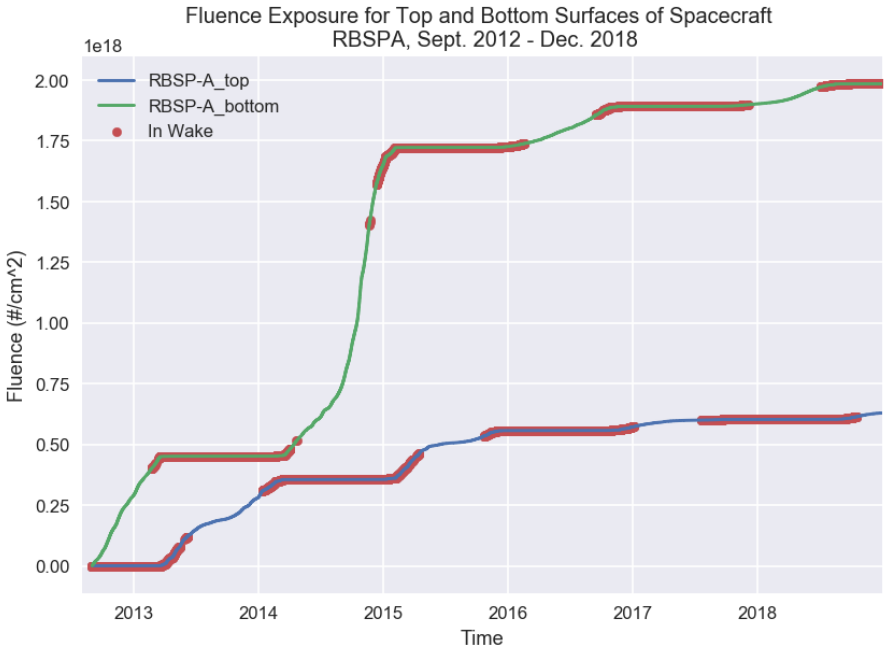

Figure 17: Plot of fluence over time for the top and bottom surfaces of the spacecraft, with wake periods denoted by the red highlighting.

The red highlighting corresponds to periods where the given surface was in the wake of the spacecraft and protected from atomic Oxygen exposure, as defined by the L - v_{sc} dot product. The red highlighted regions also correspond to the flat segments of each graph, which symbolize negligible fluence accumulation due to the near zero atomic Oxygen flux (the flux is the time derivative of fluence).

Figure 17 shows that the top surface was in the wake of the spacecraft during the region of increased atomic Oxygen density, protecting it from intense exposure. This resulted in the bottom surface of the spacecraft experiencing nearly four times the fluence than that of the top, before the perigee-lowering portion of the mission. Consequently, we'd expect the surface of EFW sensor 6 to degrade more than sensor 5, resulting is different I-V characteristics for each sensor and thus less accurate electric field measurements using these two sensors.

4 Discussion

It is known that atomic Oxygen exposure changes DAG-213 coated surfaces (Samaniego et al., 2019), so it is illuminating to calculate that impact in the context of this model. We can approximate the amount of degradation to a small patch of the DAG-213 coated spheres using the end of mission fluence value calculated above. In this approximation, we will assume that each atomic Oxygen particle has a 100% "hit rate", meaning that it will interact with exactly one Carbon atom suspended in the DAG-213 coating and remove it from the surface. Using the worst case scenario surface (section 3.1), before the perigee lowering occurred, the fluence value was 5.28×10^{18} atoms/cm^2. Thus for a 1 cm $\times$ 1 cm patch of DAG-213, 5.28×10^{18} atomic Oxygen atoms impinged the surface.

DAG-213 Density	0.984 g/cm^3
Graphite Content of DAG-213 by Weight	28%
Molar Mass of Carbon	12 g/mol

Table 1: DAG-213 Specs, retrieved from Ladd Research Industries (2018)

Table 1 shows the composition and density of DAG-213, which will be used to determined the mass loss of DAG-213. The mass of Carbon per cm thickness of coating in a 1 cm $\times$ 1 cm patch of DAG-213 is:

$$\frac{0.984 \text{ g DAG-213}}{1 \text{ cm}^3 \text{ DAG-213}} \times \frac{28 \text{ g C}}{100 \text{ g DAG-213}} \times (1 \text{ cm} \cdot 1 \text{ cm}) = 0.276 \text{ g C/cm}$$

Converting this to Carbon atoms per cm of DAG-213 coating:

$$0.276 \frac{\text{g C}}{\text{cm DAG}} \times \frac{1 \text{ mol}}{12 \text{ g C}} \times \frac{6.022 \times 10^{23} \text{ atoms}}{\text{mol}} \times \frac{1 \text{ cm}}{10000 \ \mu\text{m}} = 1.385 \times 10^{18} \text{ C atoms}/\mu\text{m}$$

Combining this result with the end of mission fluence gives the approximate loss of coating per 1 cm $\times$ 1 cm patch of DAG-213:

$$\frac{5.28 \times 10^{18} \text{atoms}}{1.385 \times 10^{18} \text{atoms}/\mu\text{m}} \approx 3.8 \mu\text{m}$$

The typical thickness of the DAG-213 coating applied to the sensors on the Van Allen Probes is on the order of 5-15 μm. Even in the worst case scenario, the calculated atomic

Oxygen fluence would not result in total erosion of the coating to the sphere surface. However, as shown in section 3.4, surfaces with different orientations with respect to the spacecraft's velocity experience different magnitudes of atomic Oxygen exposure, and thus different levels of material degradation. The unevenness of a single spheres coating could play a role in the less accurate readings observed towards the end of the mission.

In addition, total erosion of a sphere's DAG-213 coating may not be necessary to produce the observed sensor degradation. In a study on the effects of ultraviolet irradiation on low earth orbit (LEO) spacecraft surfaces, it was found that UV photons, the radiation responsible for the photoemission of electrons from the sensor surfaces, normally travel up to a depth of 0.1 μm in material (Wu et al., 2014). This implies that surface irregularities within the top 0.1 μm of the DAG-213 coating may play the largest role in the photoemission properties of the EFW sensors. Thus, the assumption that the atomic Oxygen particles have a 100% hit rate may not be necessary for the modeled atomic Oxygen fluence to produce the observed sensor degradation.

This is explored in Figure 18, where the fluence over time plot from Figure 7 is shown, with dashed lines denoting the points along the mission when 0.1 μm of DAG-213 coating would be eroded by atomic Oxygen. Each vertical line corresponds to a different hit rate, ranging from 100% to 3%. The erosion necessary to affect the sensor photoemssion could have occurred as early as one month into the mission, given the conditions represented in Figure 18. However, a more conservative estimation would have the degradation occurring during the second half of the mission. Regardless, it is likely that at least 0.1 μm of DAG-213 was eroded from the sensor surface during the mission given the results of this model.

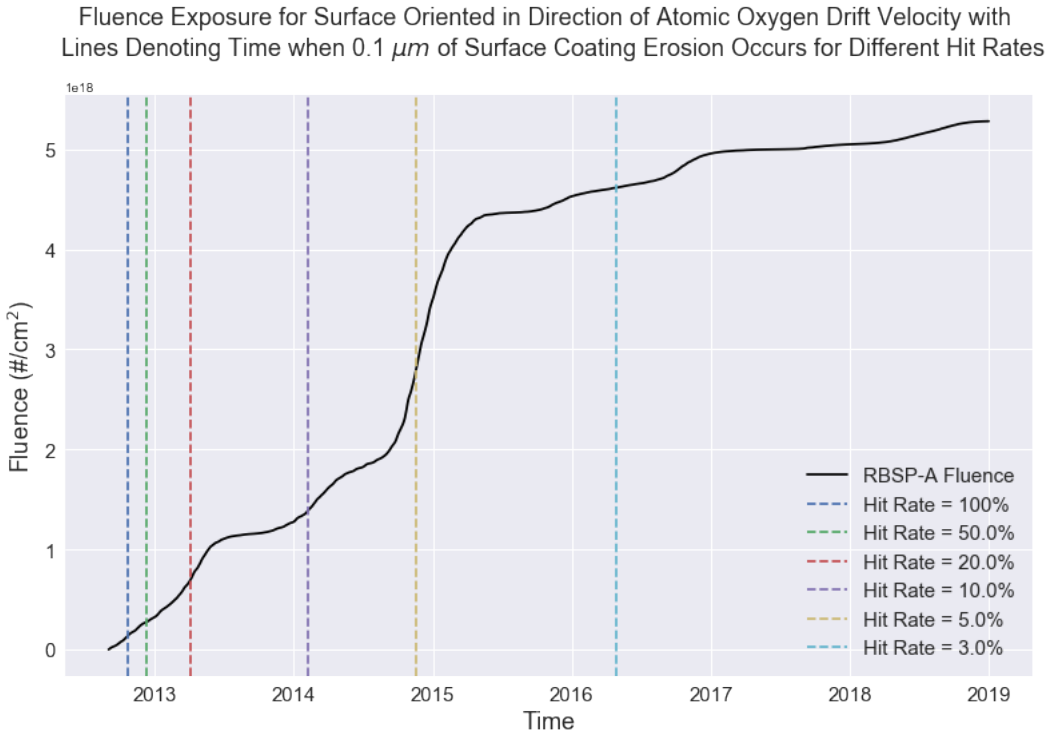

Figure 18: RBSP-A fluence accumulation before perigee lowering, with lines denoting the times when 0.1 μm erosion first occurred, given different hit rates.

5 Conclusions

The calculations and result presented in this paper tell us a lot about the varying conditions of the different surfaces of the Van Allen Probes. It is clear that not all surfaces of the spacecrafts are equal; some are exposed to substantially different atomic Oxygen environments than others due to their orientation with respect to the spacecraft motion. However, space weather plays a substantially large role in the atomic Oxygen density and exposure as well. Day-side perigee passes that occur during the solar maximum result is the largest accumulation of fluence, and are thus potentially the most damaging to the spacecraft. In addition, a minor factor to consider is temperature of the atomic Oxygen plasma that the gas that the spacecraft is immersed in. At higher gas temperatures, previously shielded surfaces are no longer safe.

This study also provides insight into ways of reducing atomic Oxygen exposure. Tracking the Sun cycle can help protect particularly vulnerable surfaces. Aligning them in the wake of the spacecraft during these time periods can drastically mitigate their exposure. In additional, exposure can be reduced in the spacecraft's perigee is kept primarily on the night side of the Earth during periods of solar maximum. This can be done with careful mission design and planning.

The methods developed in this paper can be applied to any spacecraft orbit if the orbit parameters are known. This can help plan future missions where atomic Oxygen exposure would present issues with the spacecraft operation. This can also be used to analyze past missions to determine the if atomic Oxygen exposure resulted in sensor or spacecraft surface degradation.

Acknowledgments

The data used in this paper is available via the Van Allen Probes website (`http://rbspgway.jhuapl.edu`). In addition, space weather data was collected via the Space Weather Prediction Center at the National Oceanic and Atmospheric Adminastration (`https://www.swpc.noaa.gov/communities/space-weather-enthusiasts`). The authors thank the scientists and engineers associated with the EFW instrument for providing the high-quality data reported in this paper. They are also thankful to the developers of the the NRLMSISE-00 Python package (Joshua Milas and Dr. Dominik Brodowski, information available at `https://www.brodo.de/space/nrlmsise/` and `https://ccmc.gsfc.nasa.gov/modelweb/atmos/nrlmsise00.html`) and the HWN93 Python package (Michael Hirsch and A. E. Hedin, information available at `https://ccmc.gsfc.nasa.gov/modelweb/atmos/hwm.html`). The work by the EFW team was conducted under NASA contract NNN06AA01C.

References

Acton, C. (1996). Ancillary data services of nasa's navigation and ancillary information facility. *Planetary and Space Science*, *44*(1), 65 - 70.

Banks, B. A., Groh, K. K. D., & Miller, S. K. (2004). Low earth orbital atomic oxygen interactions with spacecraft materials. *MRS Proceedings*, *851*. doi: 10.1557/proc-851-nn8.1

Bonnell, J., et al. (2008). The electric field instrument (efi) for themis. *Space Science Reviews*, *141*(1-4), 303–341. doi: 10.1007/s11214-008-9469-2

Bourassa, R., & Gillis, J. (1992). Atomic oxygen exposure of ldef experiment trays. *NASA Contractor Report*.

Fuhrmann, P. A. (1984). Robotic manipulators and the product of exponentials formula. In *Mathematical theory of networks and systems. proceedings of the international symposium held at the ben gurion university of the negev, beer sheva, june 20-24, 1983.* Springer-Verlag.

Graham, W. (2007). The physics and chemistry of plasmas for processing textiles

and other materials. In *Plasma technologies for textiles* (p. 3–24). Woodhead Publishing.

Hapgood, M. (1992). Space physics coordinate transformations: A user guide. *Planetary and Space Science*, *40*(5), 711 - 717. doi: https://doi.org/10.1016/0032-0633(92)90012-D

Hathaway, D. H. (2015, Sep 21). The solar cycle. *Living Reviews in Solar Physics*, *12*(1), 4. doi: 10.1007/lrsp-2015-4

Hedin, A., Fleming, E., Manson, A., Schmidlin, F., Avery, S., Clark, R., ... Vincent, R. (1996). Empirical wind model for the upper, middle and lower atmosphere. *Journal of Atmospheric and Terrestrial Physics*, *58*(13), 1421 - 1447. doi: https://doi.org/10.1016/0021-9169(95)00122-0

Industries, L. R. (2018). `https://www.laddresearch.com/lanotattachments/download/file/id/29/store/1/ladddag213.pdf`.

NOAA. (2020). Space weather enthusiasts dashboard. `https://www.swpc.noaa.gov/communities/space-weather-enthusiasts`.

Picone, J. M., Hedin, A. E., Drob, D. P., & Aikin, A. C. (2002, Dec). Nrlmsise-00 empirical model of the atmosphere: Statistical comparisons and scientific issues. *AGU Journals*.

Samaniego, J. I., Wang, X., Andersson, L., Malaspina, D., Ergun, R. E., & Horányi, M. (2019). Investigation of coatings for langmuir probes: Effect of surface oxidation on photoemission characteristics. *Journal of Geophysical Research: Space Physics*, *124*(3), 2357–2361. doi: 10.1029/2018ja026127

SPENIVS. (2018). European space agency. `https://www.spenvis.oma.be/models.php`.

Srinivasan, D. K., Heyler, G. A., & Mcgee, T. G. (2012). Spin-axis estimation of the radiation belt storm probes spacecraft using rf doppler data. *Acta Astronautica*, *73*, 30–37. doi: 10.1016/j.actaastro.2011.12.013

Stratton, J. M., Harvey, R. J., & Heyler, G. A. (2012). Mission overview for the radiation belt storm probes mission. *The Van Allen Probes Mission*, 29–57. doi: 10.1007/978-1-4899-7433-4_3

Tapping, K. F. (2013). The 10.7 cm solar radio flux (f10.7). *Space Weather*, *11*(7), 394-406. doi: 10.1002/swe.20064

Weisstein, E. (2020). Erf. *MathWorld–A Wolfram Web Resource*. `http://mathworld.wolfram.com/Erf.html`.

Wu, J., Miyahara, A., Khan, A. R., Iwata, M., Toyoda, K., Cho, M., & Zheng, X. Q. (2014, Jan). Effects of ultraviolet irradiation and atomic oxygen erosion on total electron emission yield of polyimide. *IEEE Transactions on Plasma Science*, *42*(1), 191-198. doi: 10.1109/TPS.2013.2288699

Wygant, J., Bonnell, J., & Goetz, K. (2013, Nov). The electric field and waves instruments on the radiation belt storm probes mission. *Space Science Reviews*, *179*(1-4), 183–220. doi: 10.1007/s11214-013-0013-7

Wygant, J., Harvey, P. R., Pankow, D., & Mozer, F. S. (1992). Crres electric field/langmuir probe instrument. *Journal of Spacecraft and Rockets*, *29*(4), 601–604. doi: 10.2514/3.25507

100nm_erosion_plot.

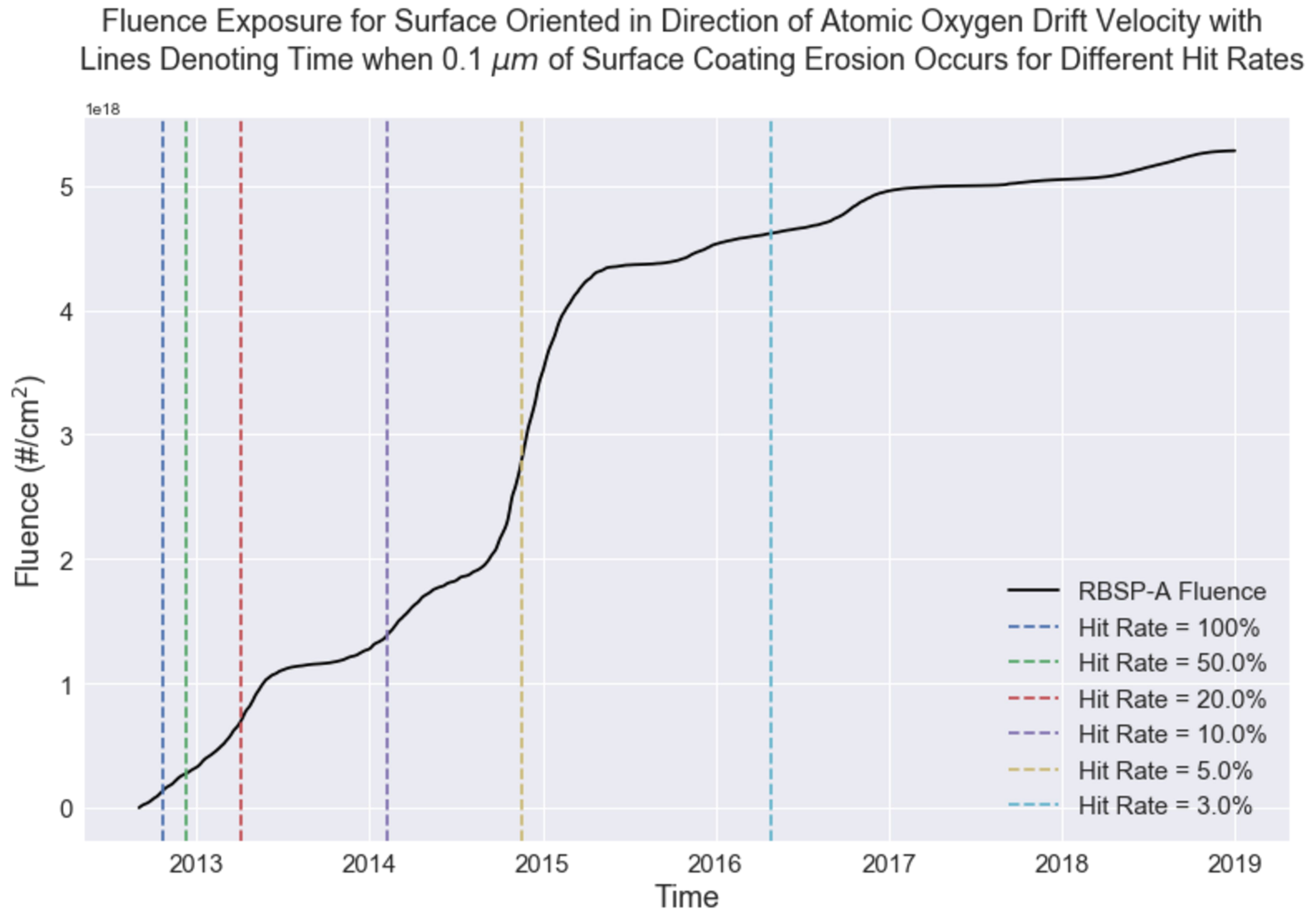
Fluence Exposure for Surface Oriented in Direction of Atomic Oxygen Drift Velocity with Lines Denoting Time when 0.1 μm of Surface Coating Erosion Occurs for Different Hit Rates
1e18
5
4
3
2
1
0
Fluence (#/cm^2)
2013
2014
2015
2016
2017
2018
2019
Time
RBSP-A Fluence
Hit Rate = 100%
Hit Rate = 50.0%
Hit Rate = 20.0%
Hit Rate = 10.0%
Hit Rate = 5.0%
Hit Rate = 3.0%

perigee_density_alt_plot.

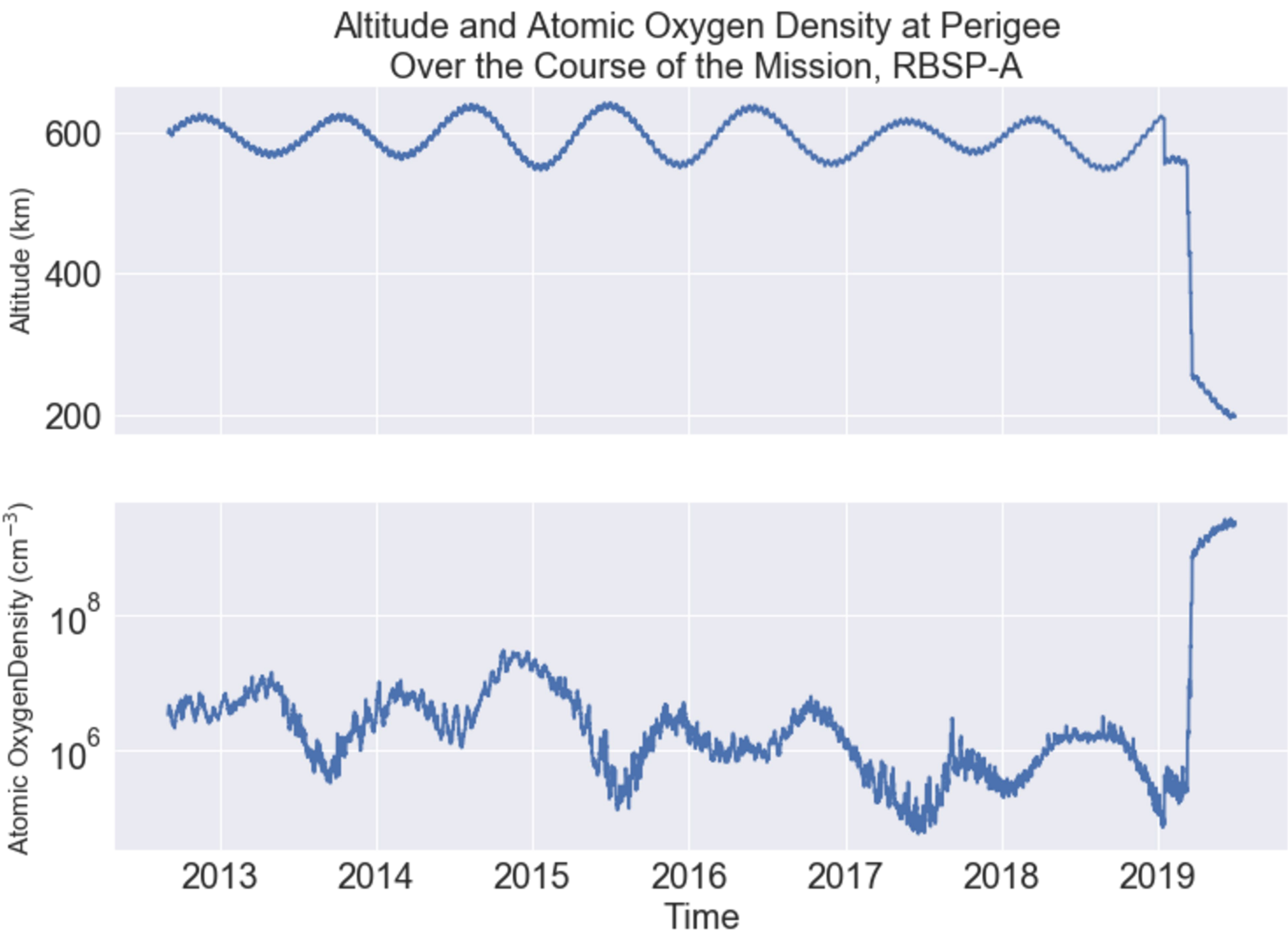
Altitude and Atomic Oxygen Density at Perigee
Over the Course of the Mission, RBSP-A
Altitude (km)
600
400
200
Atomic OxygenDensity (cm^{-3})
10^8
10^6
2013
2014
2015
2016
2017
2018
2019
Time

fluence_plot.

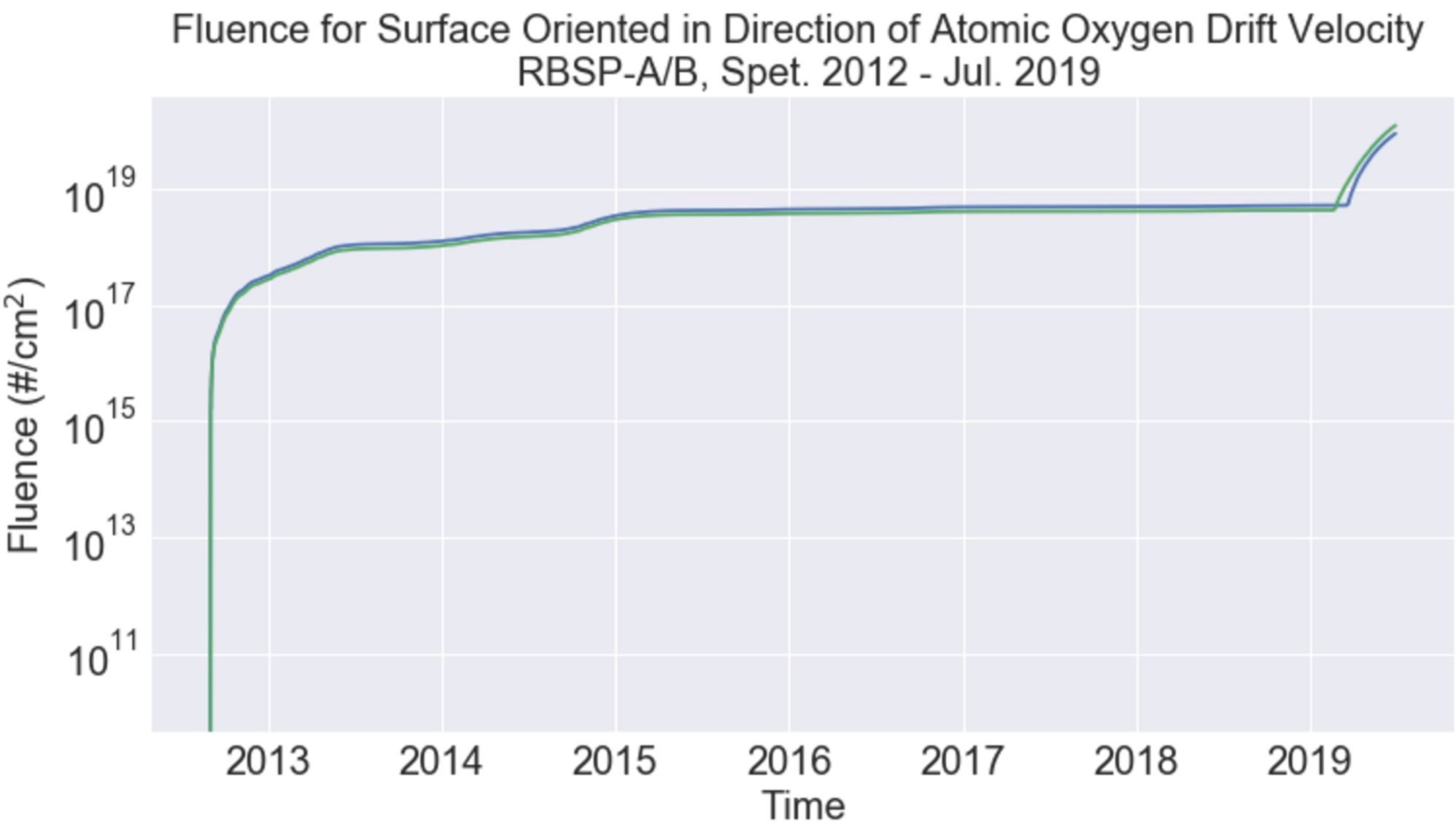
Fluence for Surface Oriented in Direction of Atomic Oxygen Drift Velocity
RBSP-A/B, Spet. 2012 - Jul. 2019
Fluence (#/cm²)
10^19
10^17
10^15
10^13
10^11
2013
2014
2015
2016
2017
2018
2019
Time

fluence_anti_parallel_plot.

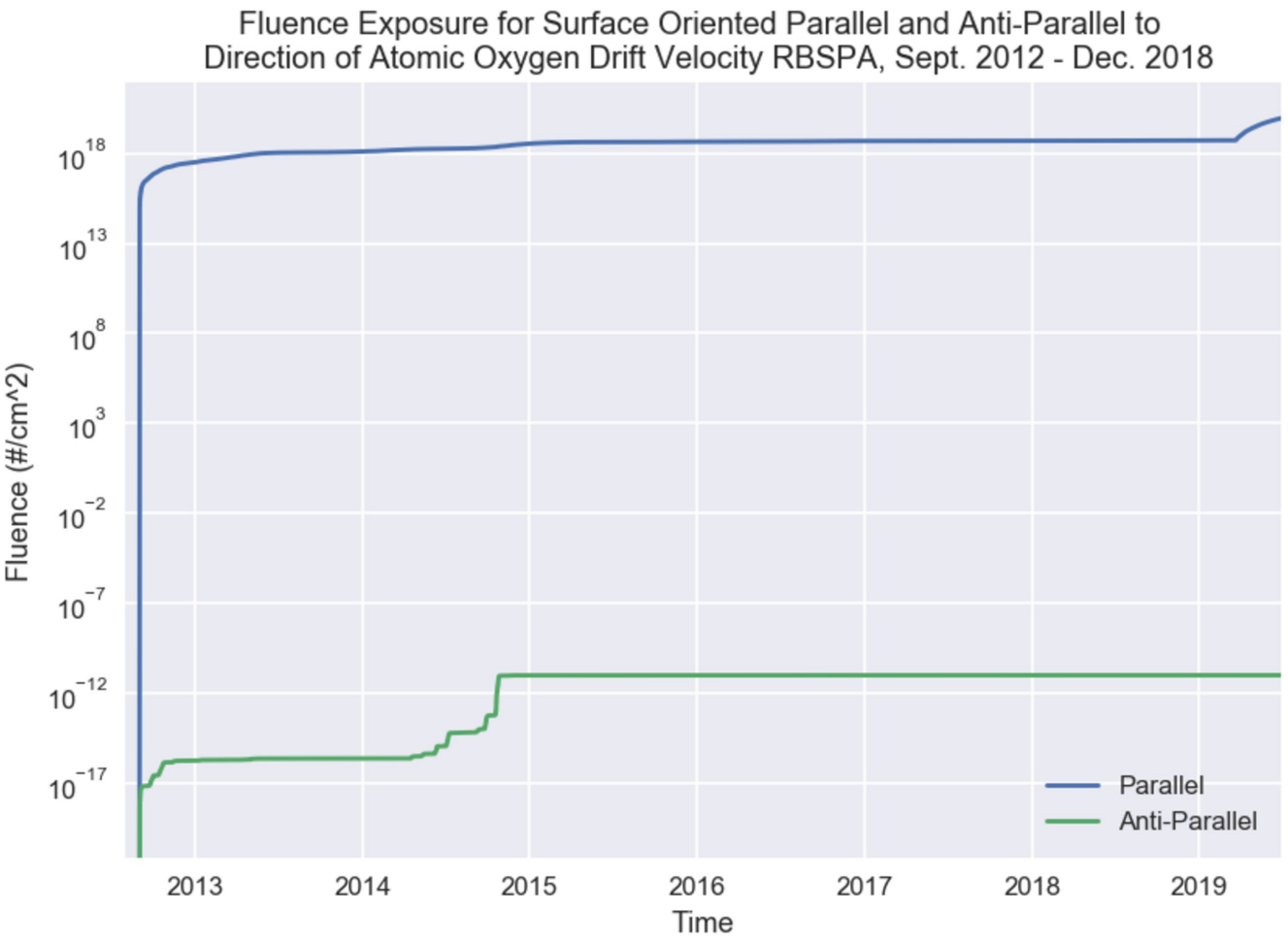
Fluence Exposure for Surface Oriented Parallel and Anti-Parallel to
Direction of Atomic Oxygen Drift Velocity RBSPA, Sept. 2012 - Dec. 2018
Fluence (#/cm^2)
10^{18}
10^{13}
10^{8}
10^{3}
10^{-2}
10^{-7}
10^{-12}
10^{-17}
2013
2014
2015
2016
2017
2018
2019
Time
Parallel
Anti-Parallel

angle_to_drift_plot.

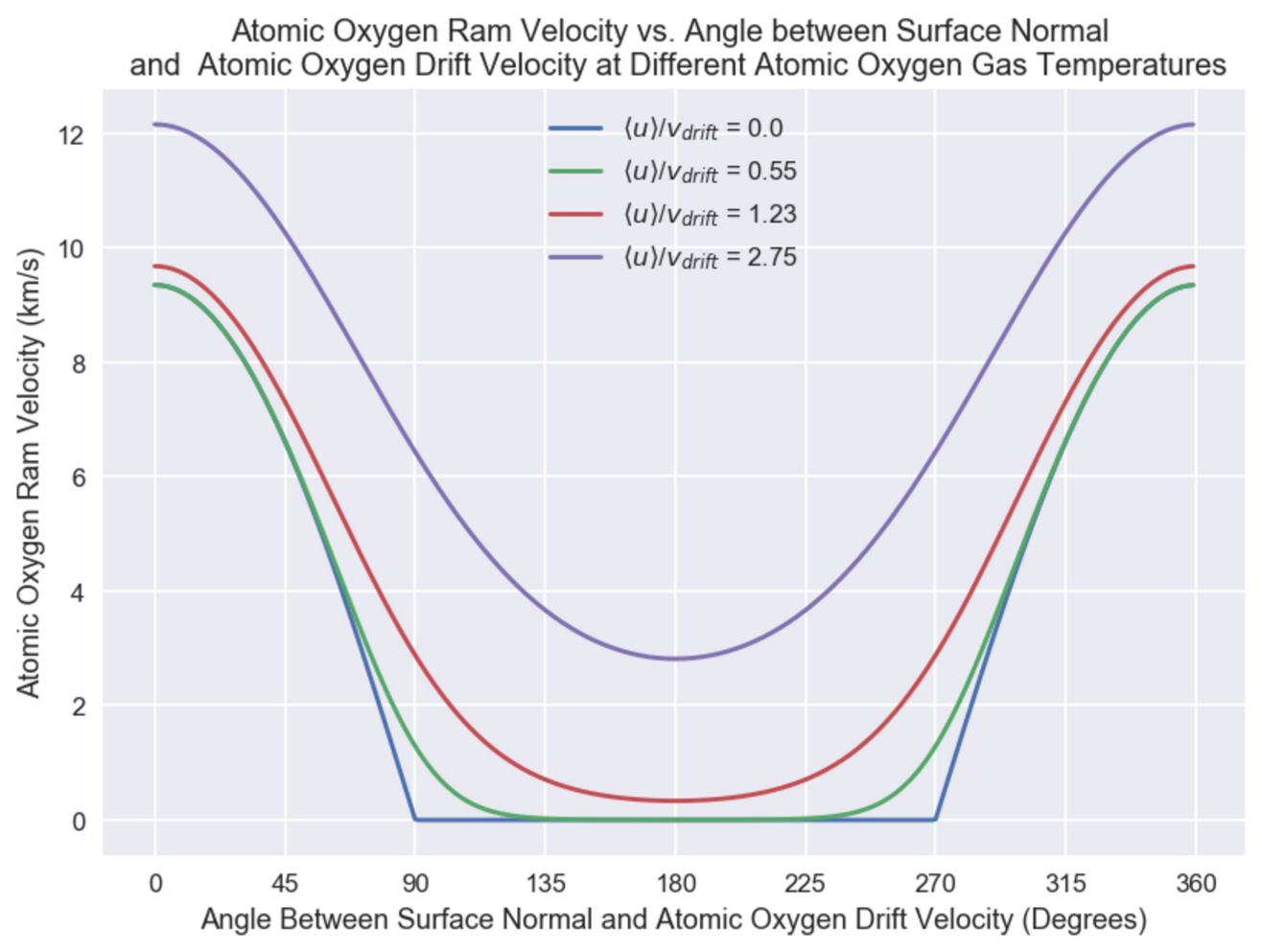
Atomic Oxygen Ram Velocity vs. Angle between Surface Normal
and Atomic Oxygen Drift Velocity at Different Atomic Oxygen Gas Temperatures
⟨u⟩/v_drift = 0.0
⟨u⟩/v_drift = 0.55
⟨u⟩/v_drift = 1.23
⟨u⟩/v_drift = 2.75
Atomic Oxygen Ram Velocity (km/s)
0
2
4
6
8
10
12
0
45
90
135
180
225
270
315
360
Angle Between Surface Normal and Atomic Oxygen Drift Velocity (Degrees)

angle_to_drift_diagram.

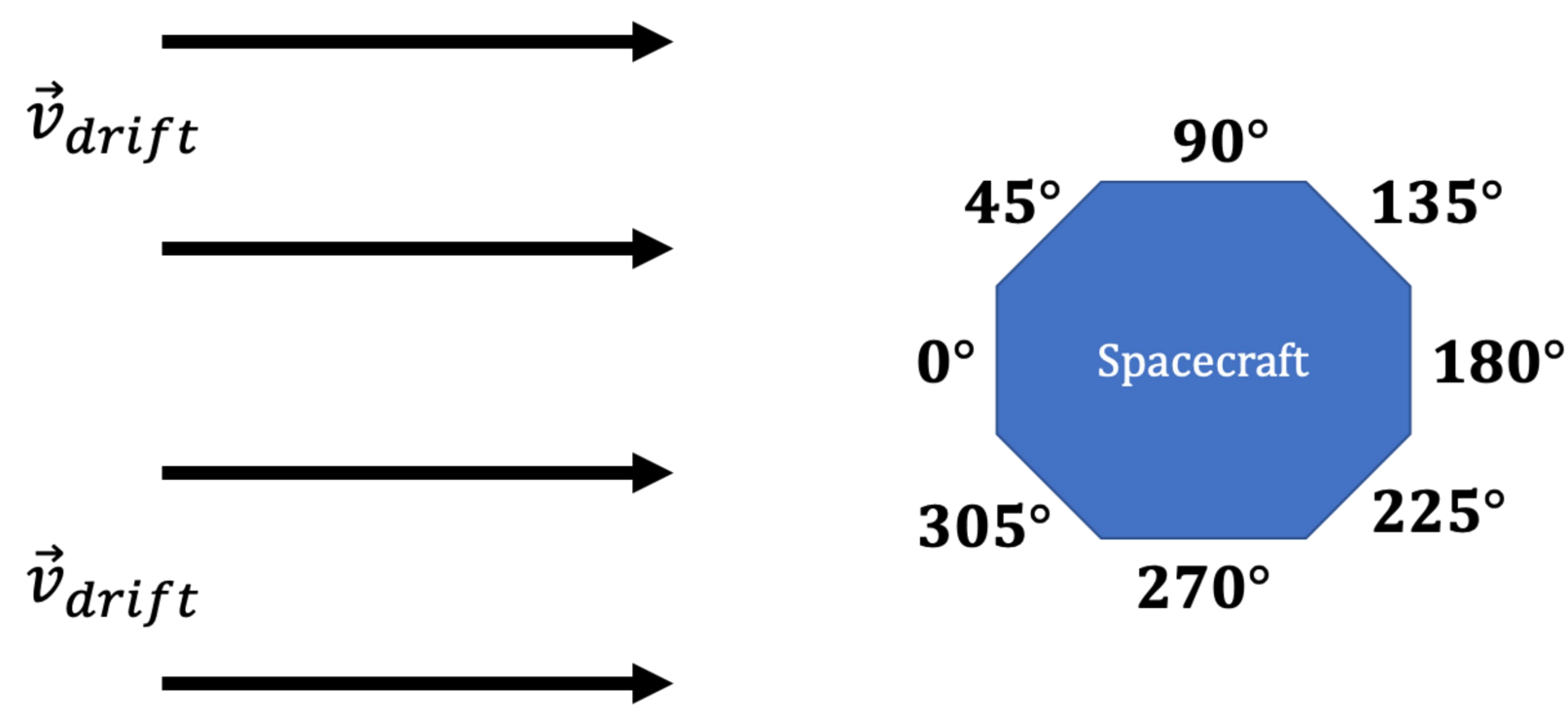
$\vec{v}_{drift}$
$\vec{v}_{drift}$
90°
45°
135°
0°
Spacecraft
180°
305°
225°
270°

pre19_density_alt_plot.

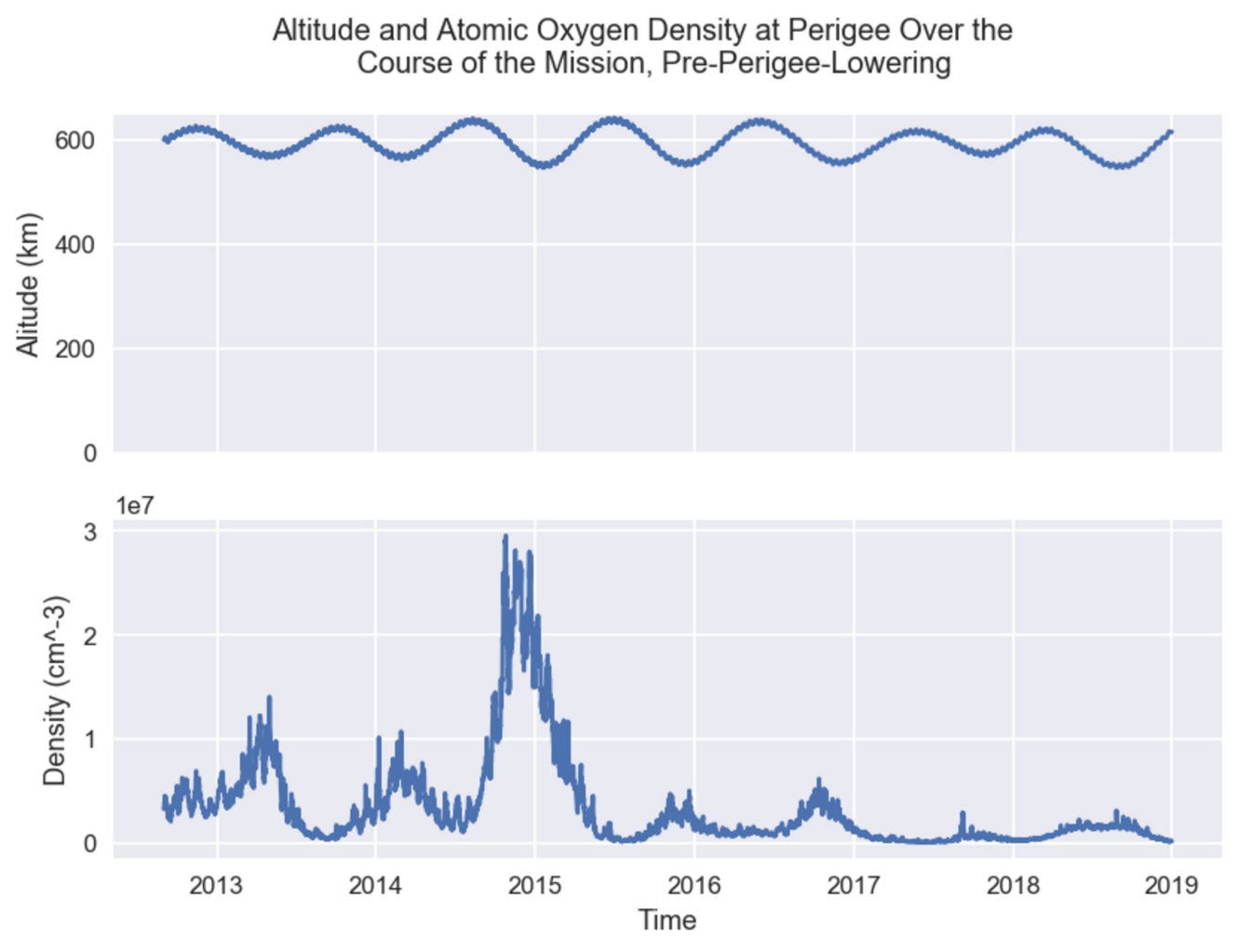
Altitude and Atomic Oxygen Density at Perigee Over the Course of the Mission, Pre-Perigee-Lowering
Alitude (km)
600
400
200
0
1e7
3
2
1
0
Density (cm^-3)
2013
2014
2015
2016
2017
2018
2019
Time

f107_gse_density_plot.

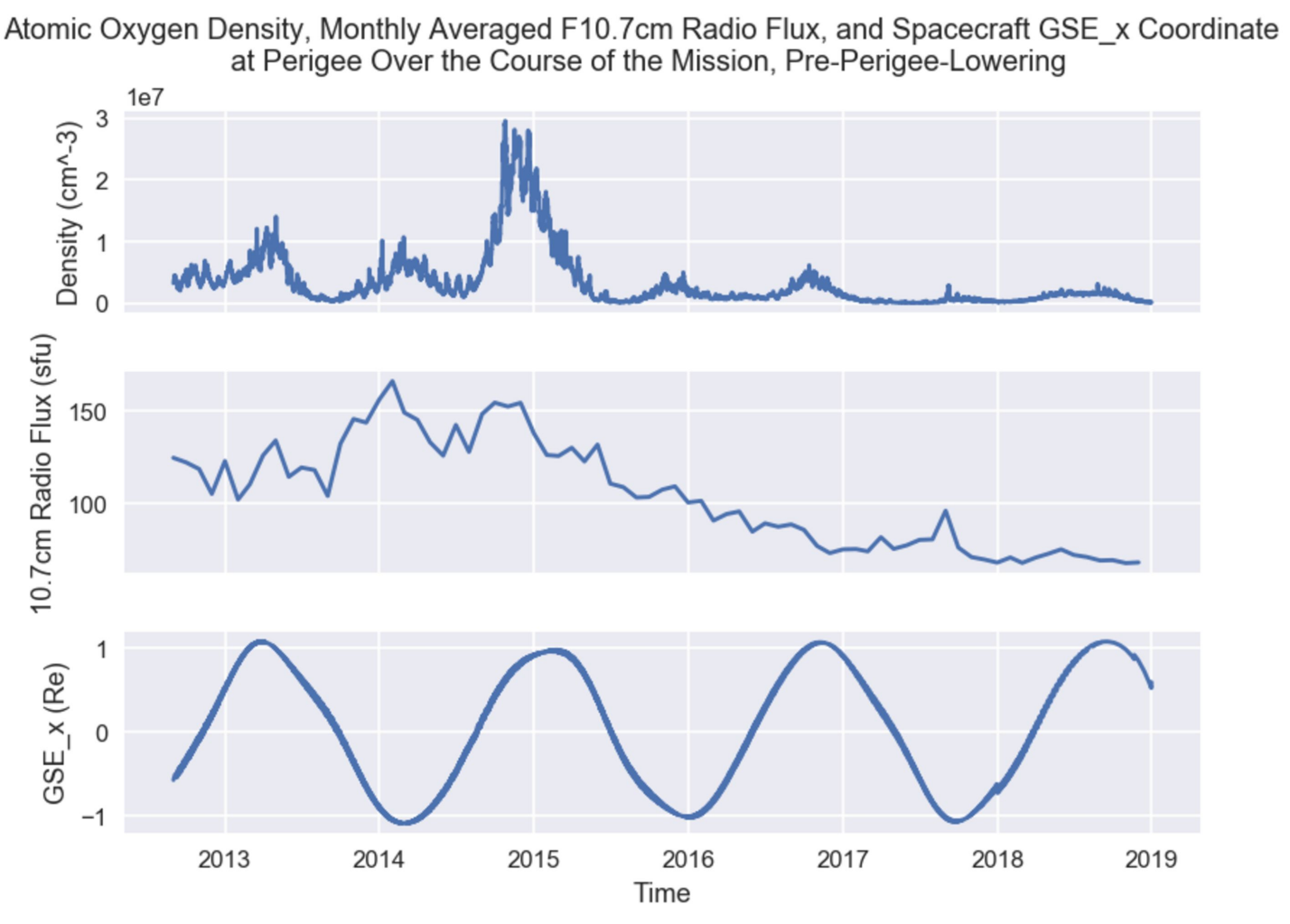
Atomic Oxygen Density, Monthly Averaged F10.7cm Radio Flux, and Spacecraft GSE_x Coordinate at Perigee Over the Course of the Mission, Pre-Perigee-Lowering
1e7
3
2
1
0
Density (cm^-3)
150
100
10.7cm Radio Flux (sfu)
1
0
−1
GSE_x (Re)
2013
2014
2015
2016
2017
2018
2019
Time

RBSP_diagram.

Spacecraft Coordinate Systems, Sensors, and Sun Sensor Heads (SSH)

Spin Axis (+Z and +W) are oriented between 15 to 27 degrees of sun direction by attitude control

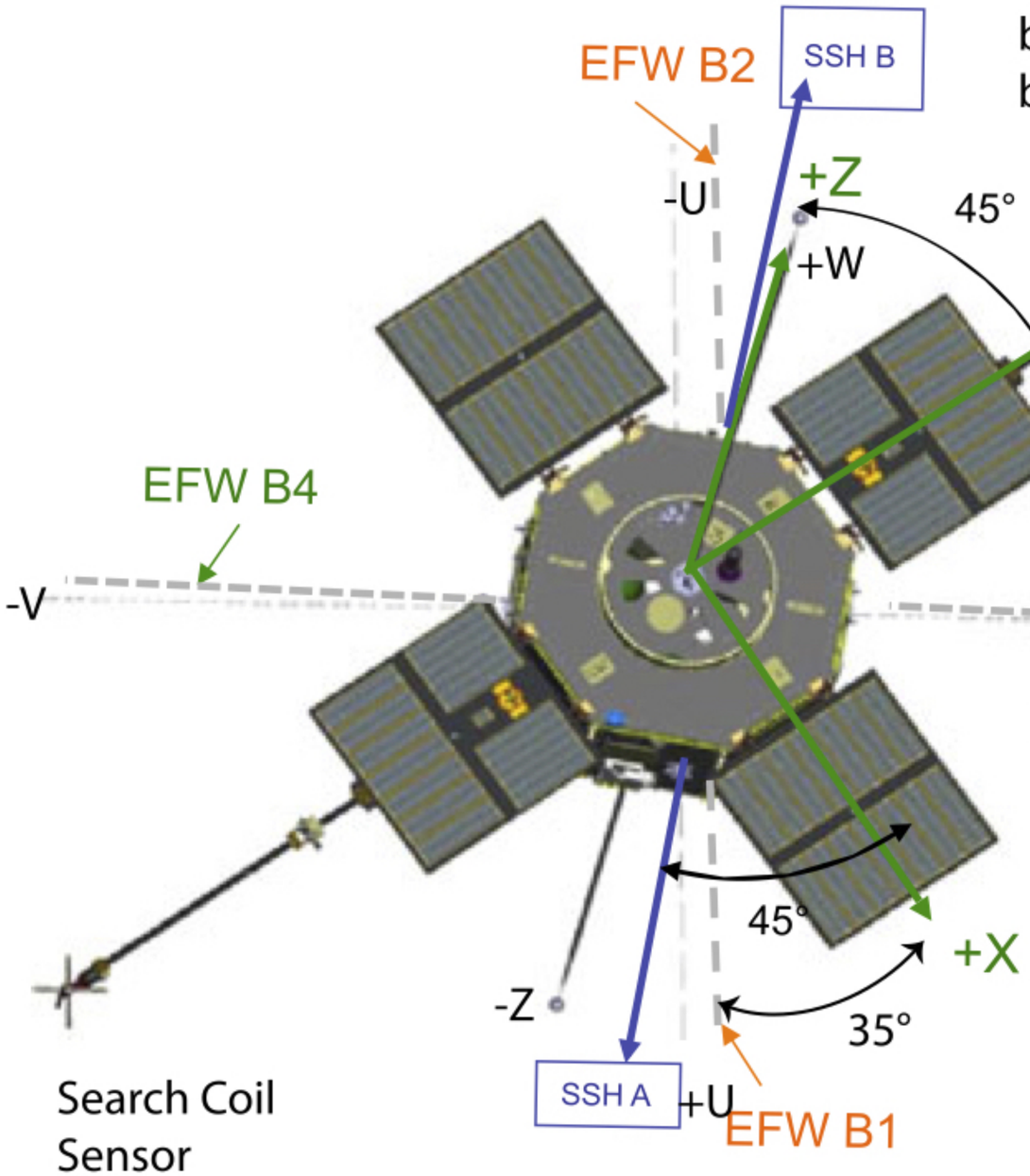

FOV of each Sun Sensor Head (SSH) is the half plane formed by the +Z axis and the and the rays labeled SSH A and SSH B in the x-y or spin plane.

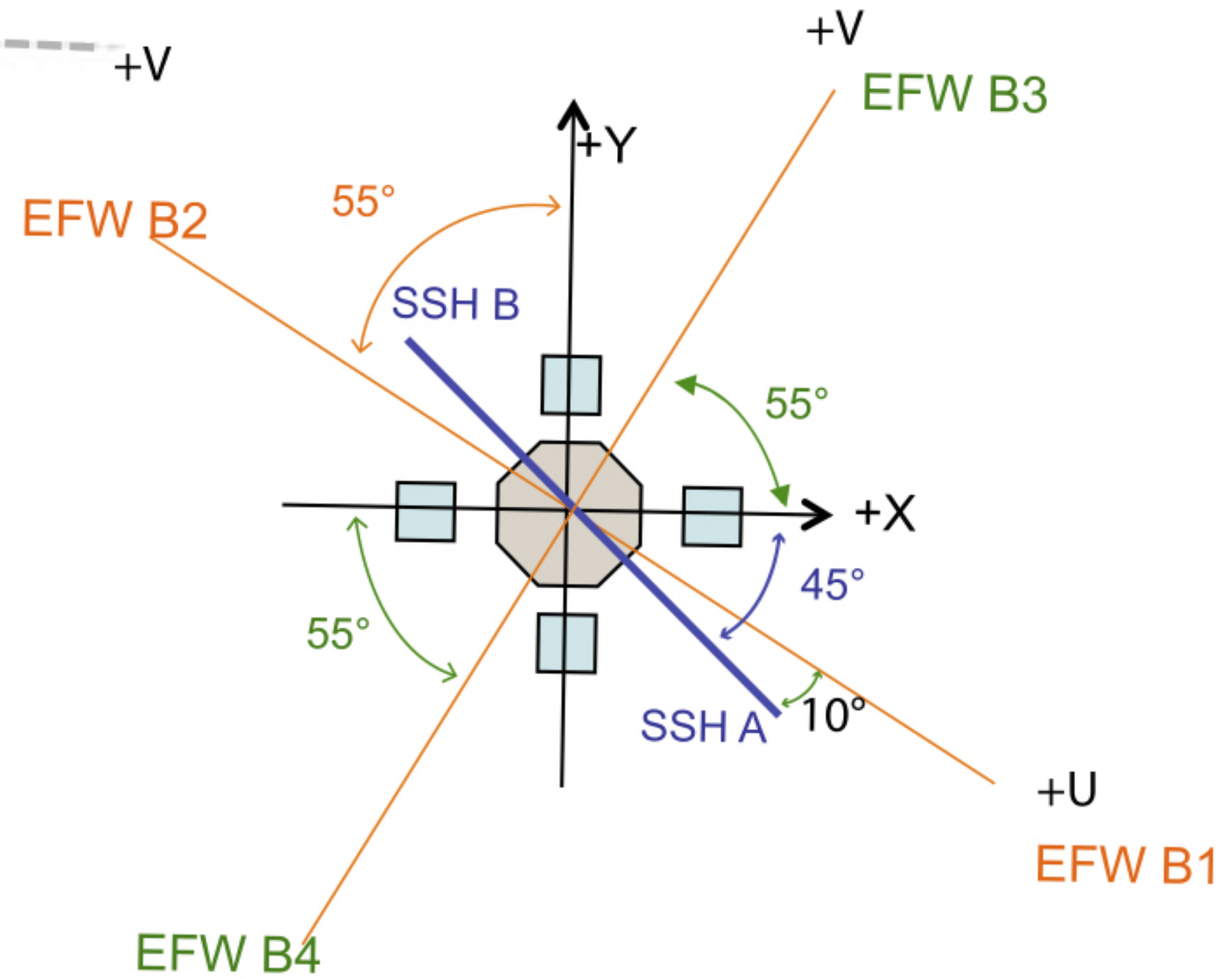

+Z and +W out of plane towards sun

orbit_1.

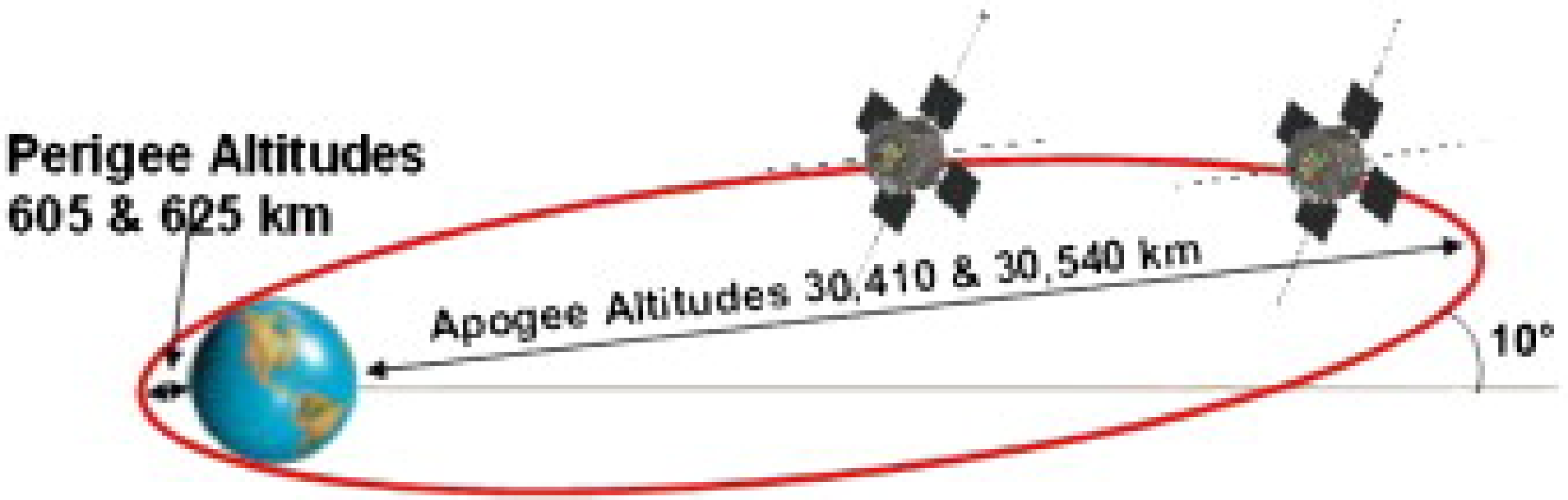
Perigee Altitudes
605 & 625 km
Apogee Altitudes 30,410 & 30,540 km
10°

orbit_2.

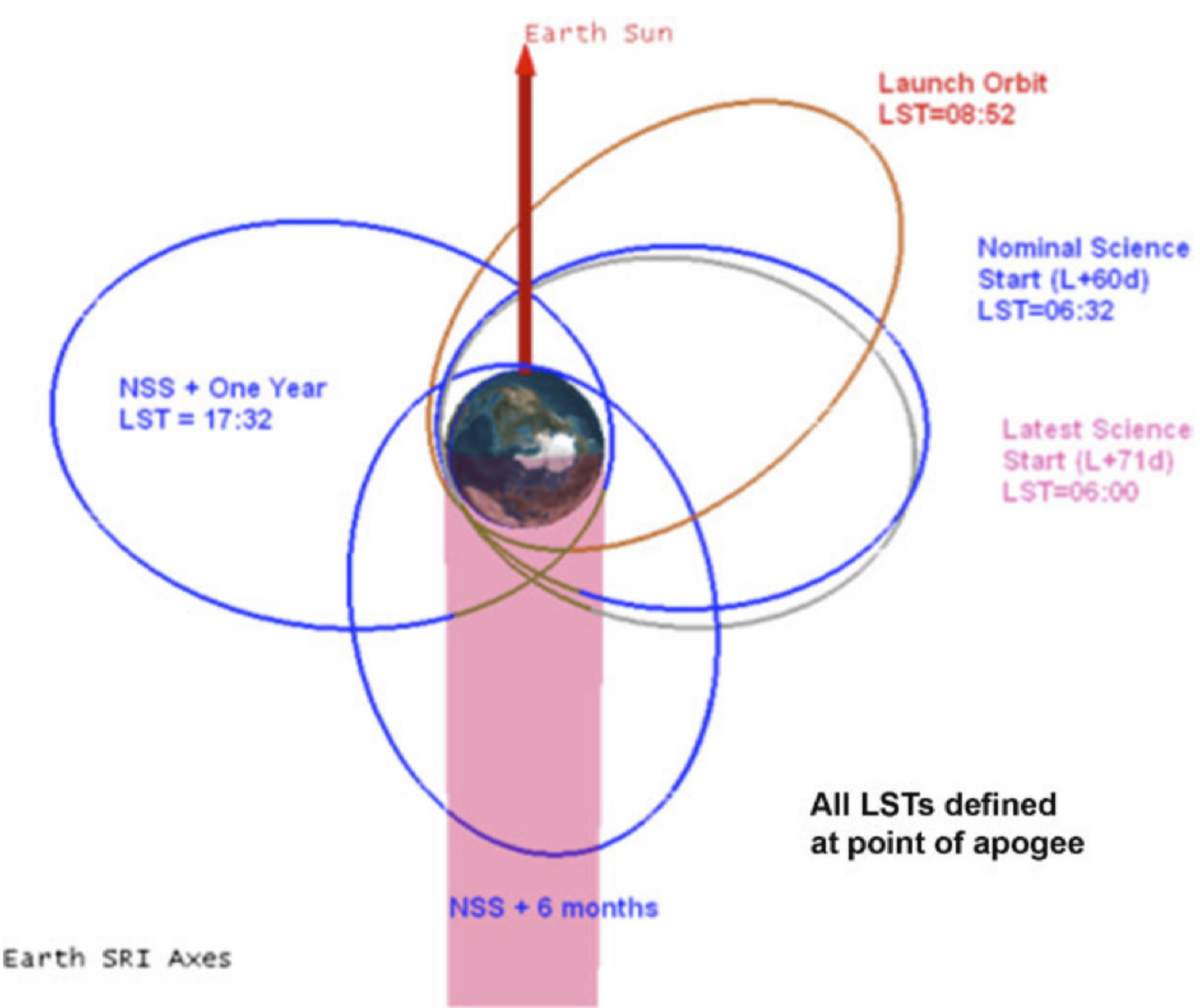
Earth Sun
Launch Orbit
LST=08:52
Nominal Science
Start (L+60d)
LST=06:32
NSS + One Year
LST = 17:32
Latest Science
Start (L+71d)
LST=06:00
All LSTs defined
at point of apogee
NSS + 6 months
Earth SRI Axes

gse_coords_diagram.

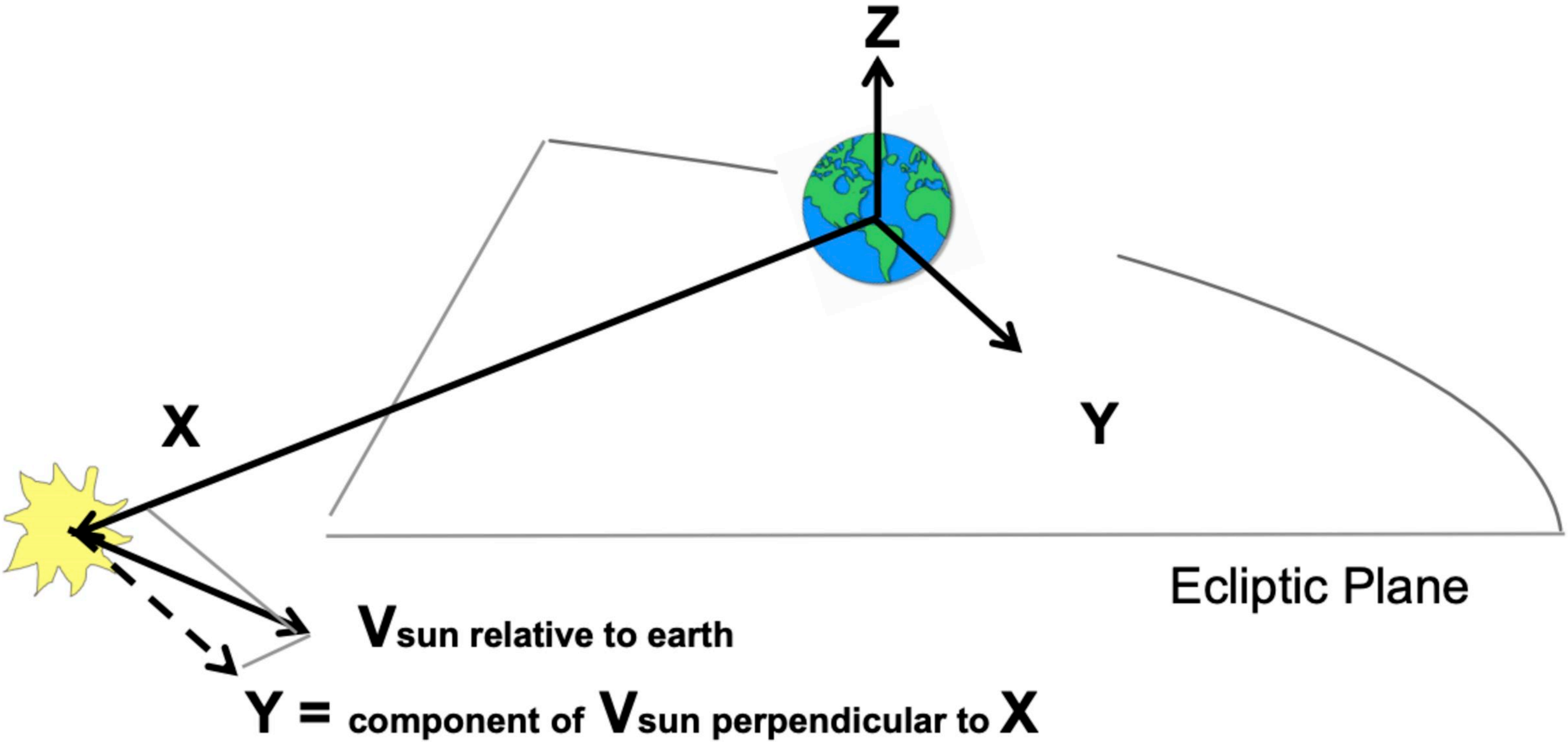
Z
X
Y
Ecliptic Plane
V sun relative to earth
Y = component of V sun perpendicular to X

post2019_fluence_plot.

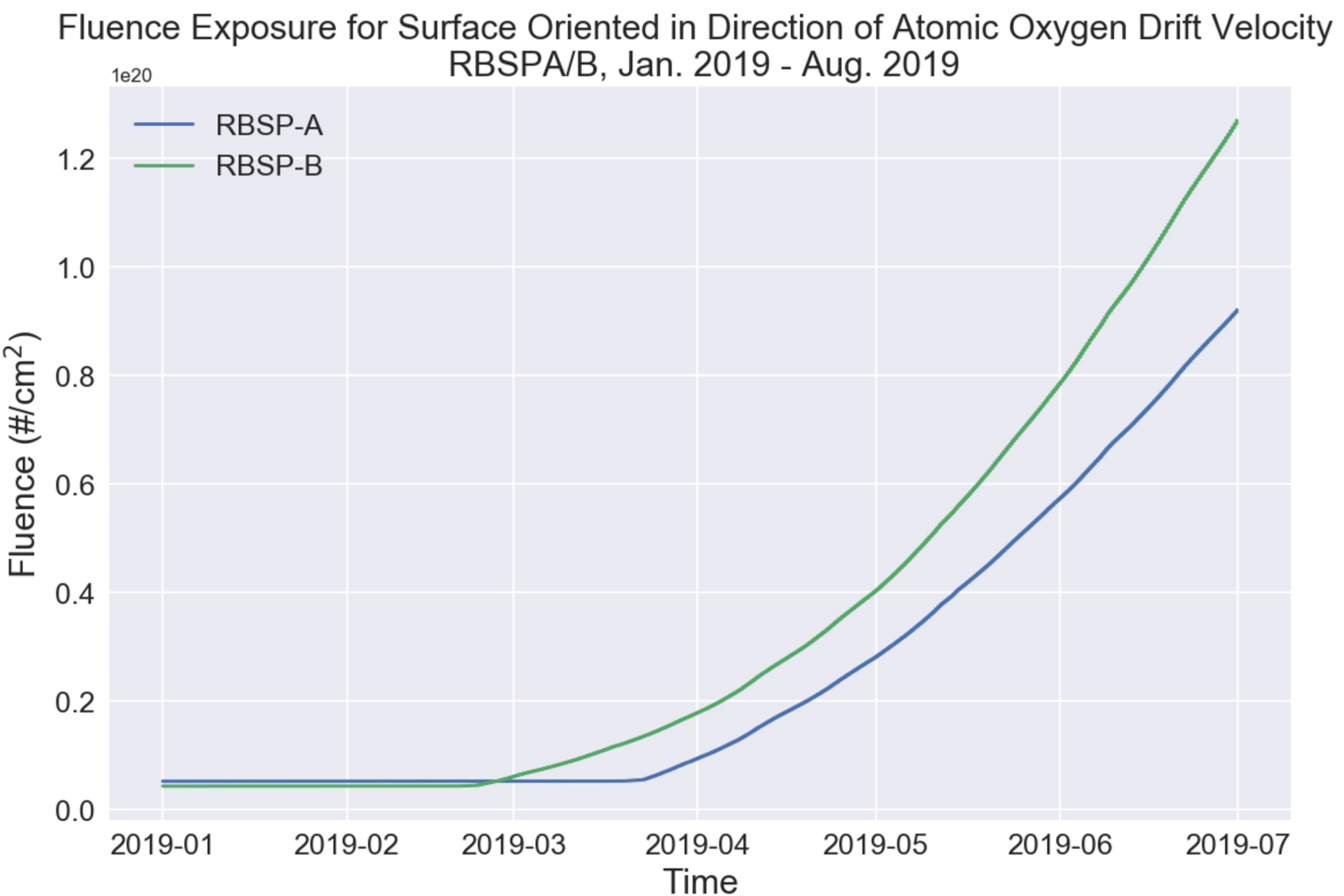
Fluence Exposure for Surface Oriented in Direction of Atomic Oxygen Drift Velocity
RBSPA/B, Jan. 2019 - Aug. 2019
1e20
RBSP-A
RBSP-B
1.2
1.0
0.8
0.6
0.4
0.2
0.0
Fluence (#/cm^2)
2019-01
2019-02
2019-03
2019-04
2019-05
2019-06
2019-07
Time

pre2019_density_alt_plot.

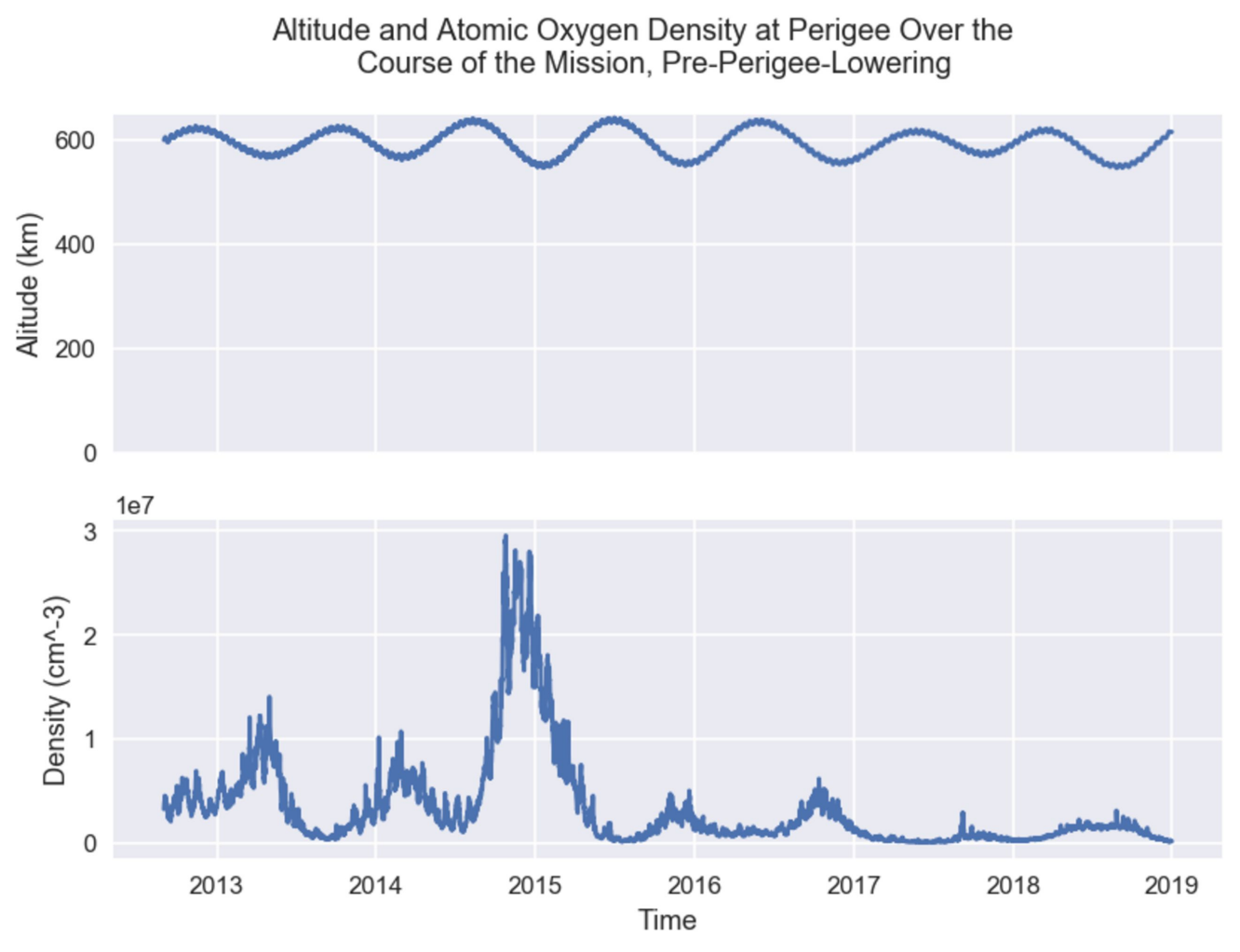
Altitude and Atomic Oxygen Density at Perigee Over the Course of the Mission, Pre-Perigee-Lowering
Alitude (km)
600
400
200
0
1e7
3
2
1
0
Density (cm^-3)
2013
2014
2015
2016
2017
2018
2019
Time

pre2019_fluence_plot.

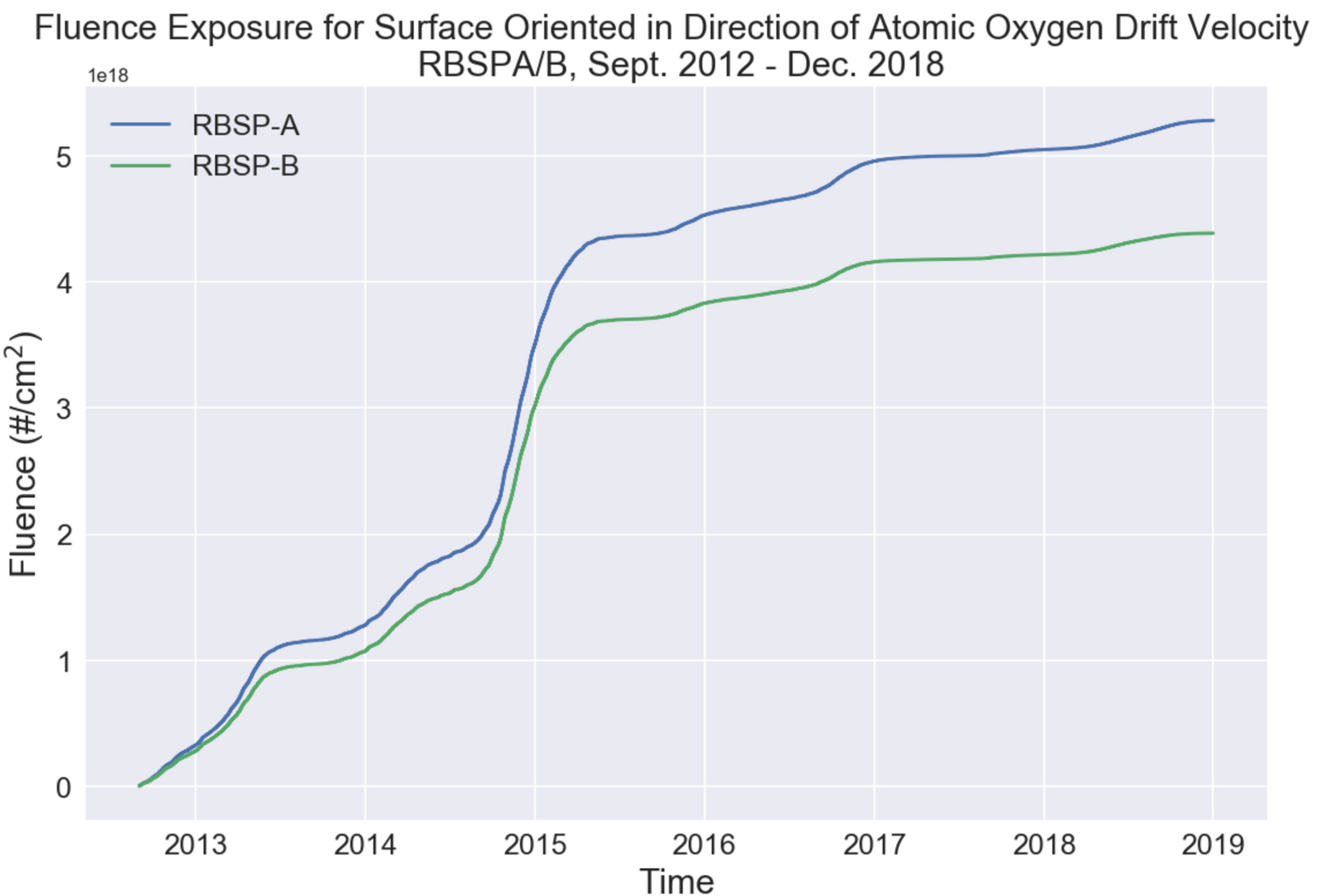
Fluence Exposure for Surface Oriented in Direction of Atomic Oxygen Drift Velocity
RBSPA/B, Sept. 2012 - Dec. 2018
1e18
RBSP-A
RBSP-B
Fluence (#/cm^2)
0
1
2
3
4
5
2013
2014
2015
2016
2017
2018
2019
Time

pre2019_fluence_a_with_lines_plot.

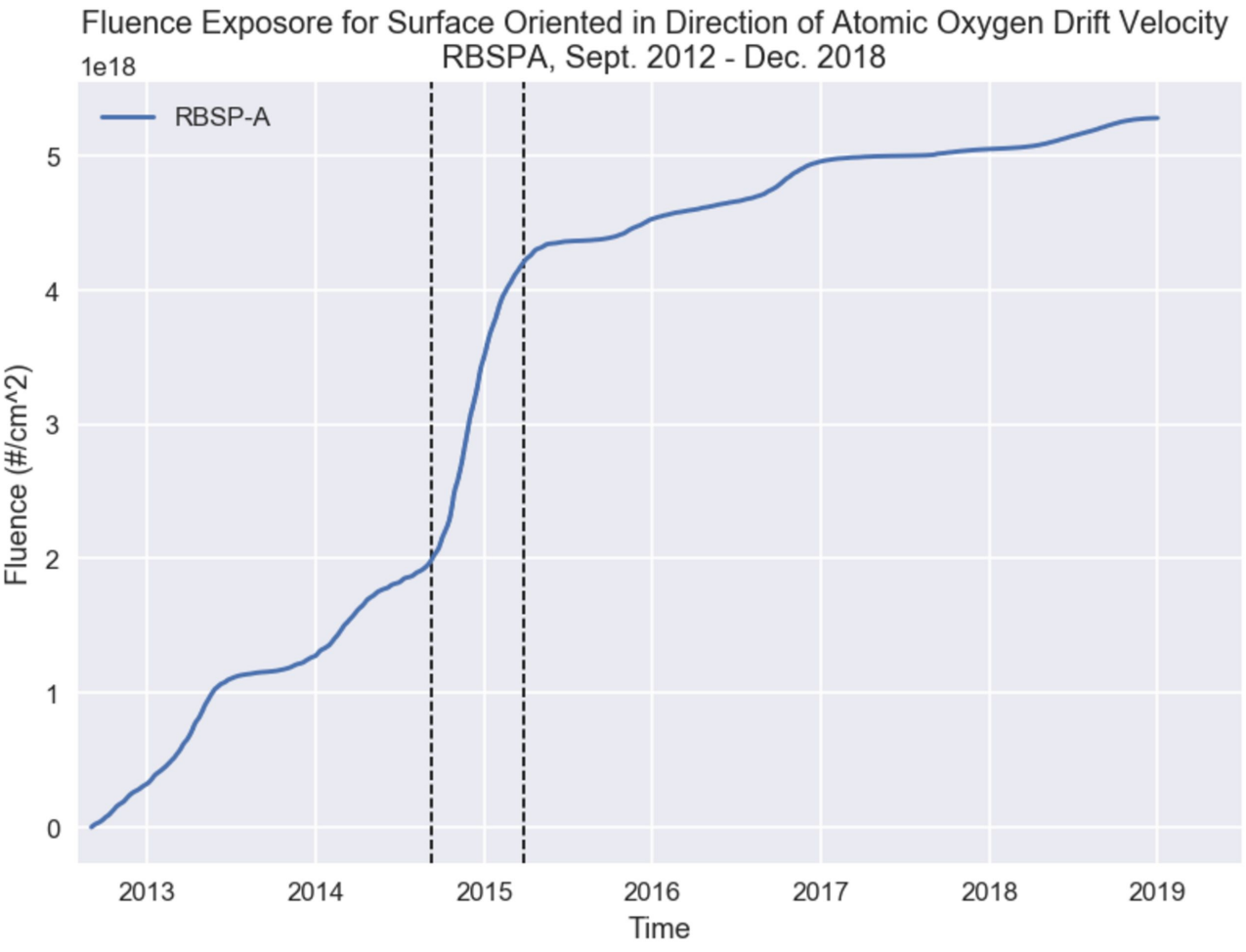
Fluence Exposore for Surface Oriented in Direction of Atomic Oxygen Drift Velocity
RBSPA, Sept. 2012 - Dec. 2018
1e18
RBSP-A
5
4
3
2
1
0
Fluence (#/cm^2)
2013
2014
2015
2016
2017
2018
2019
Time

ram_velocity_diagram_1.

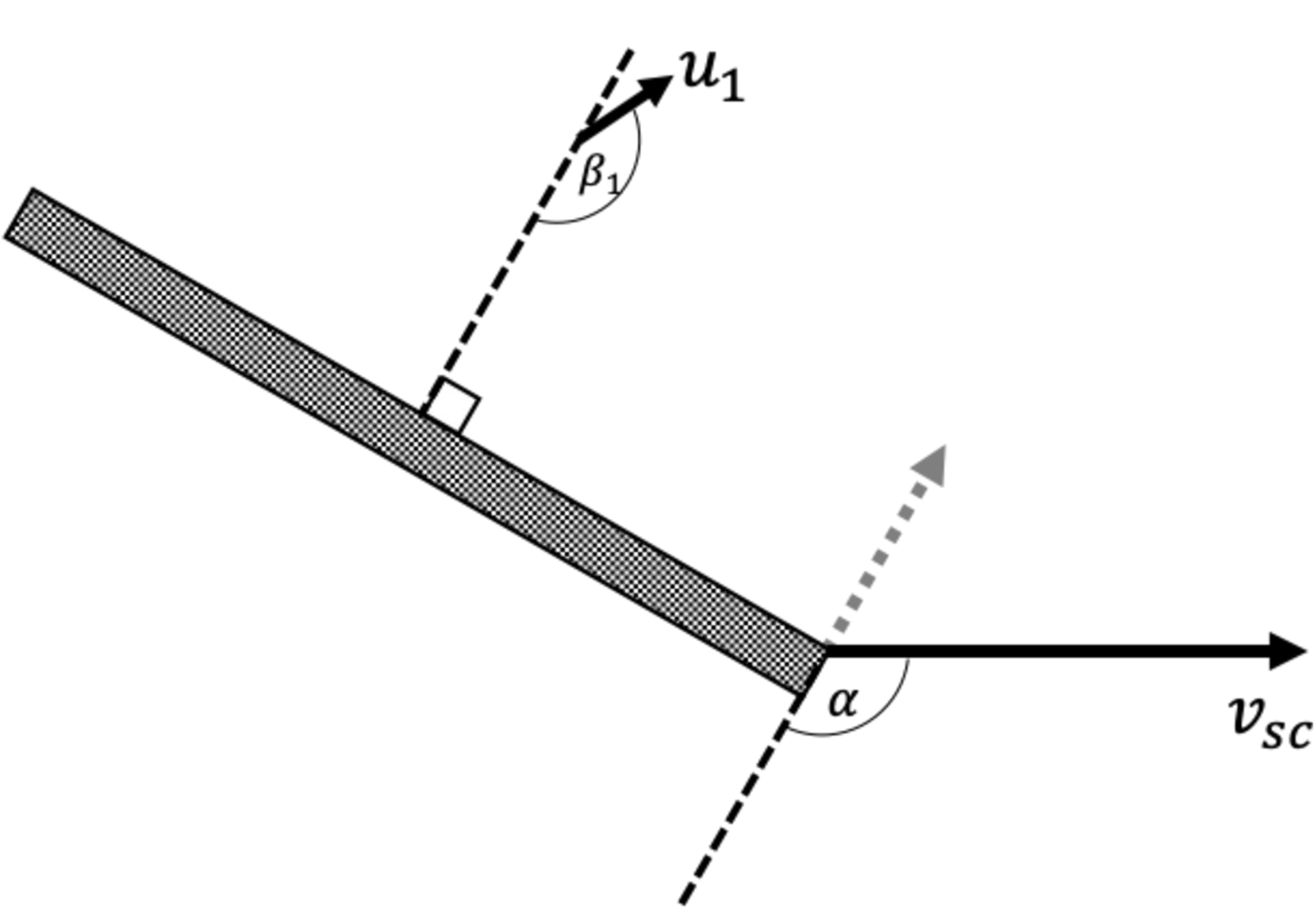
u_1
β_1
α
v_{sc}

ram_velocity_diagram_2.

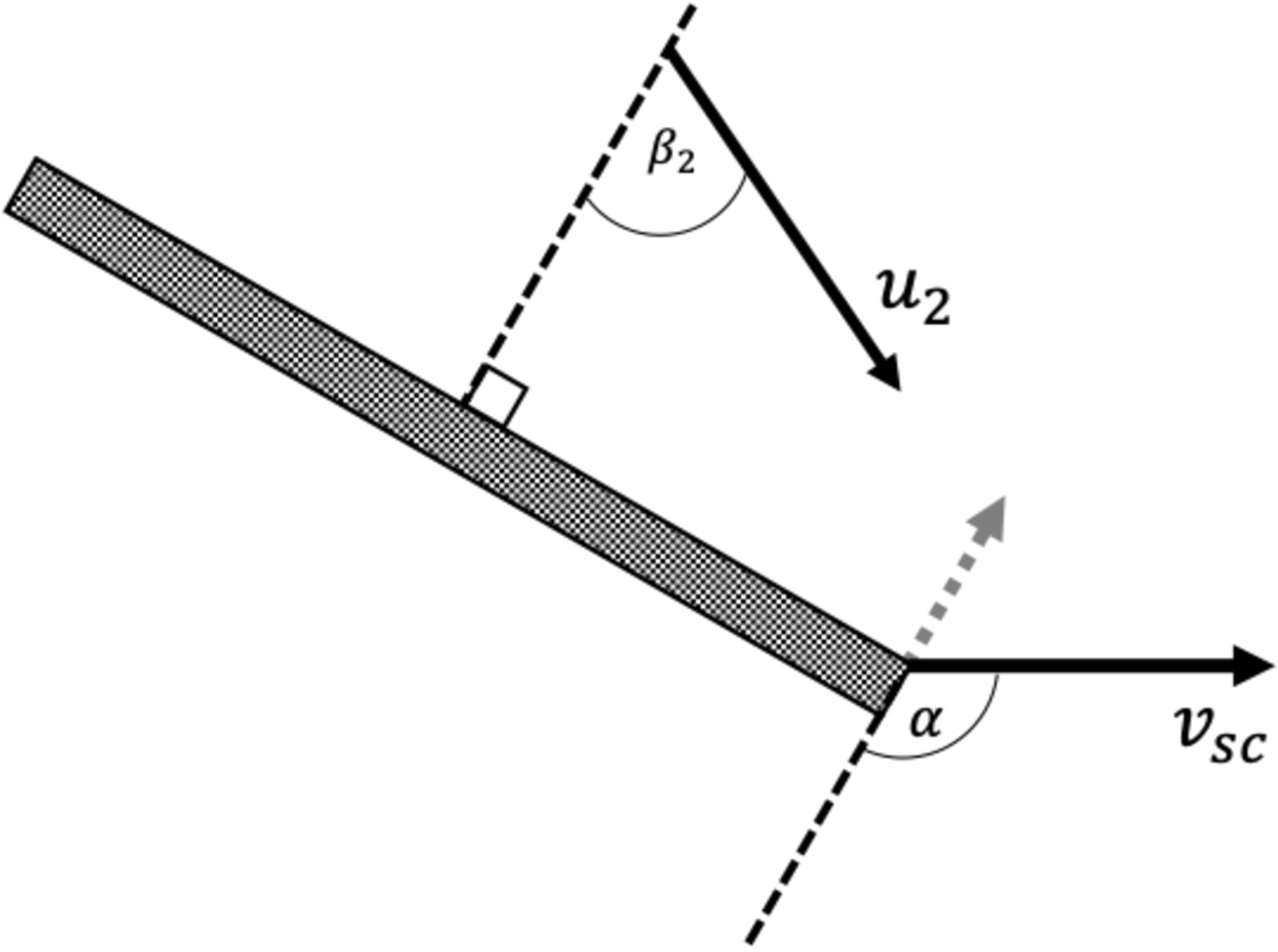
β_2
u_2
α
v_{sc}

sun_cycle.

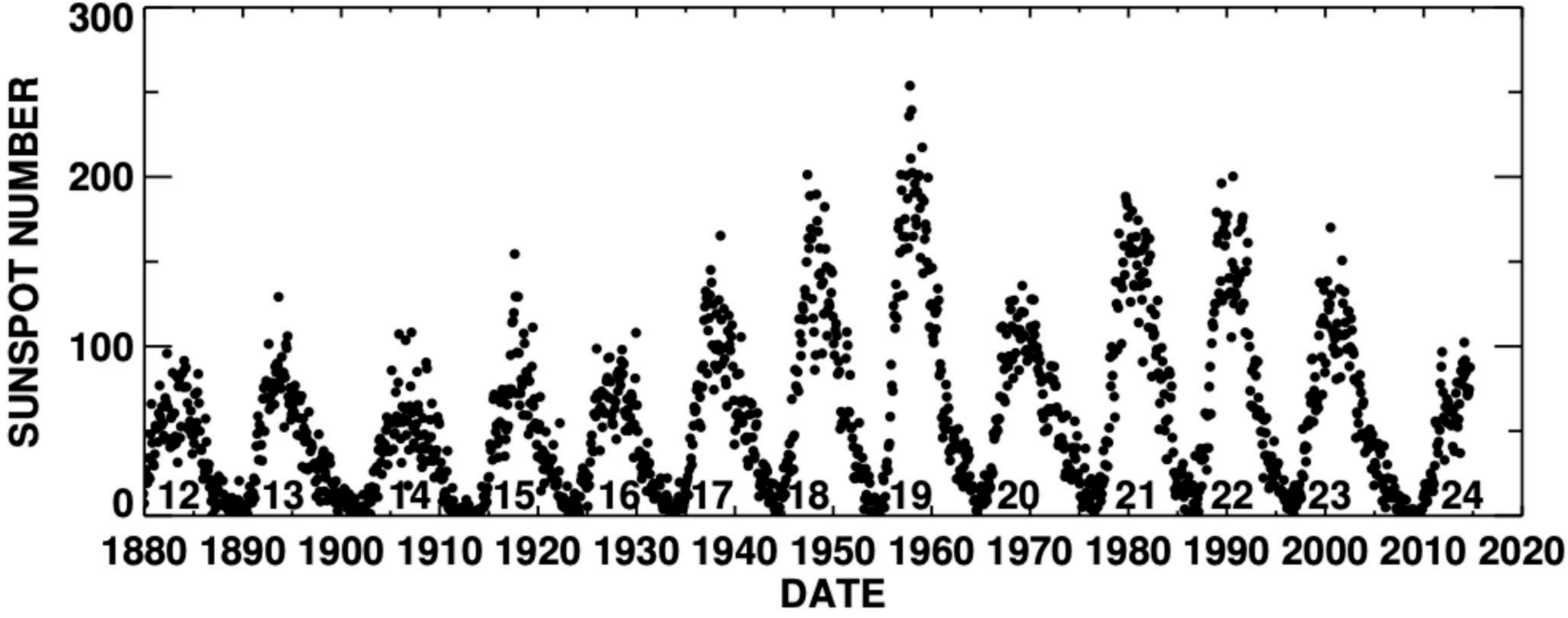
SUNSPOT NUMBER
300
200
100
0
12
13
14
15
16
17
18
19
20
21
22
23
24
1880 1890 1900 1910 1920 1930 1940 1950 1960 1970 1980 1990 2000 2010 2020
DATE

surface_diagram_rotated.

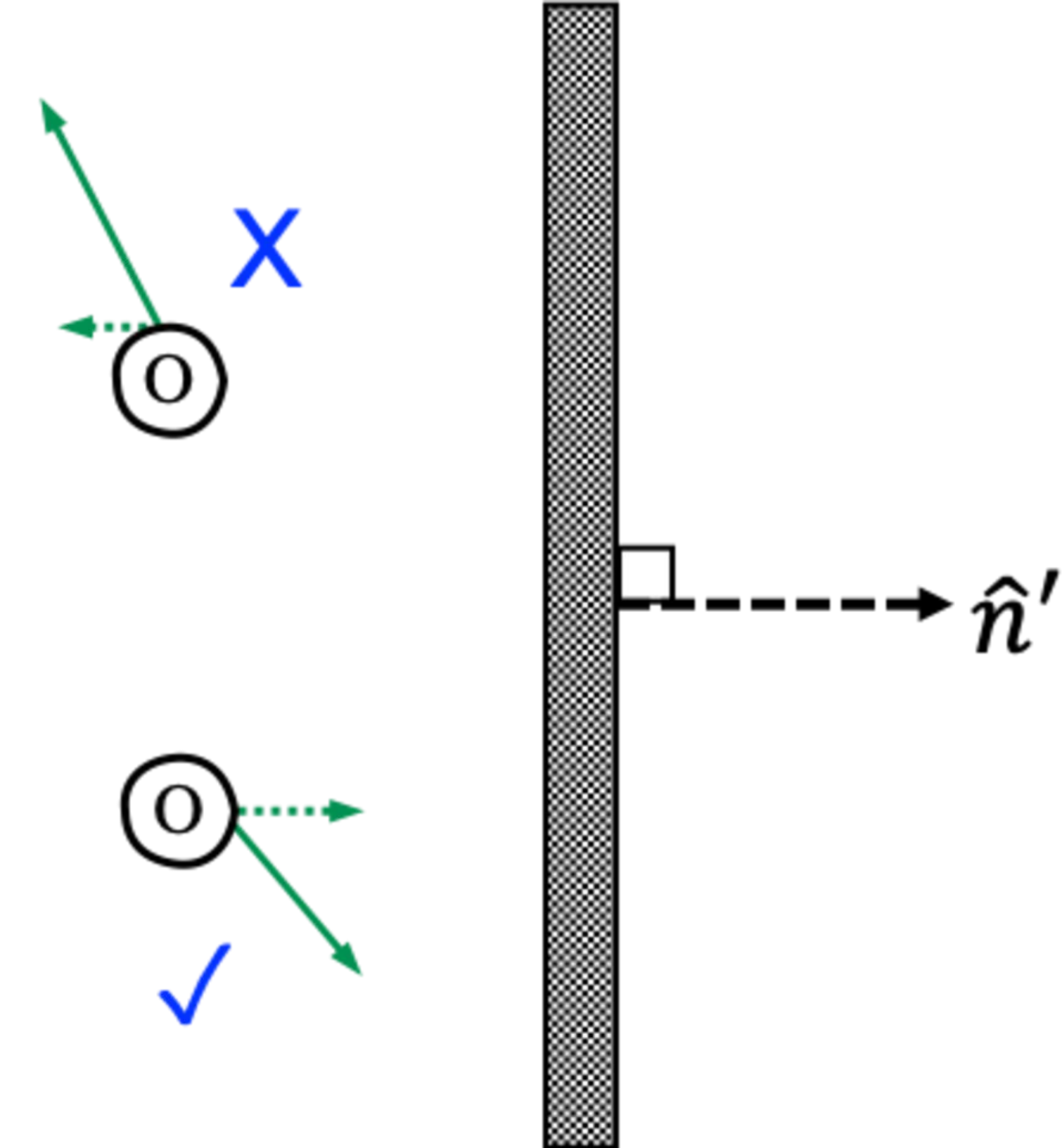
X
O
O
$\hat{n}'$

surface_diagram.

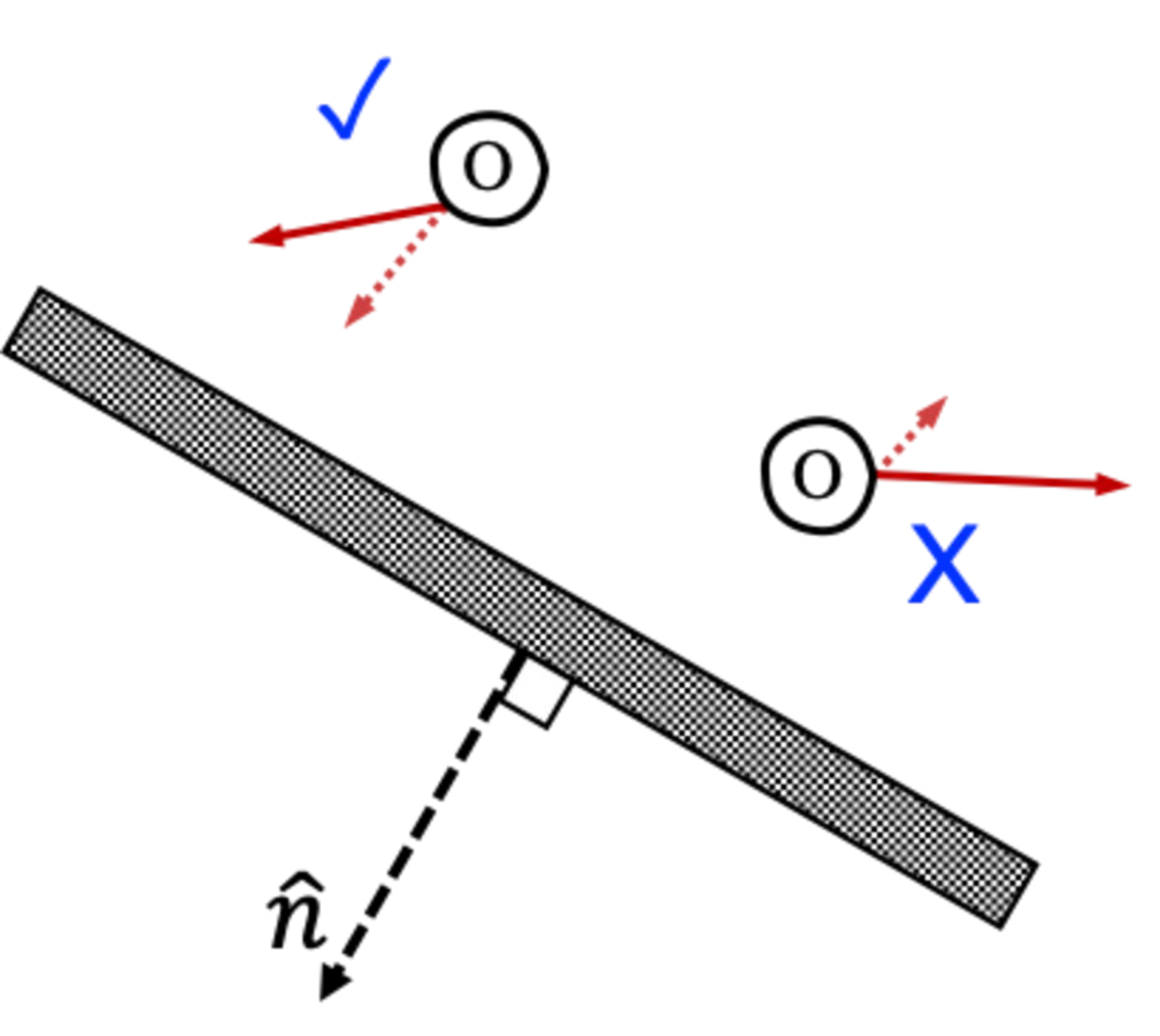
✓
O
O
X
$\hat{n}$

top_bottom_diagram.

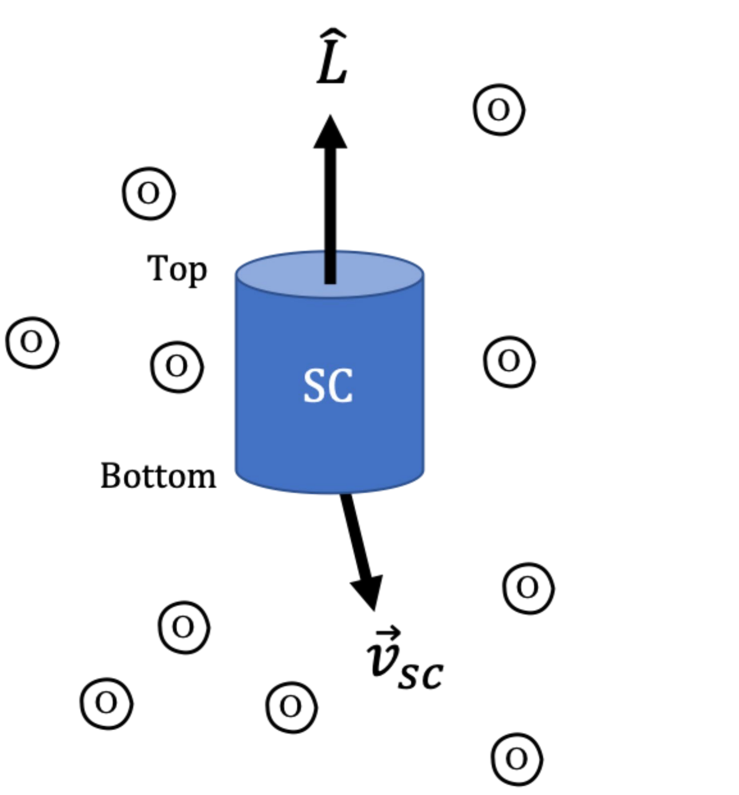

$\hat{L} \cdot \vec{v}_{sc} < 0$

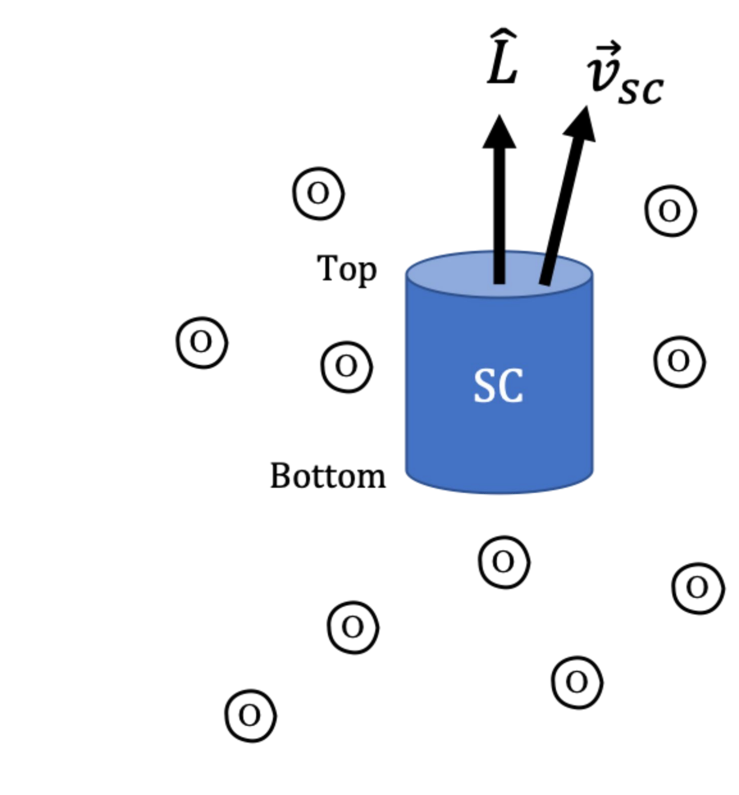

$\hat{L} \cdot \vec{v}_{sc} > 0$

10min_perigee_plots.

(A) Spacecraft Altitude

Altitude (km)

1400
1200
1000
800
600
400
200
0

(B) Atomic Oxygen Density

Number Density (cm^{-3})

3000000
2500000
2000000
1500000
1000000
500000
0

(C) Spacecraft Velocity

Velocity ($km\ s^{-1}$)

9.8
9.6
9.4
9.2
9.0
8.8
8.6

-10 -8 -6 -4 -2 0 2 4 6 8 10

Minutes Before/After Perigee on 2012-09-01 06:12:00

top_bottom_fluence_plot.

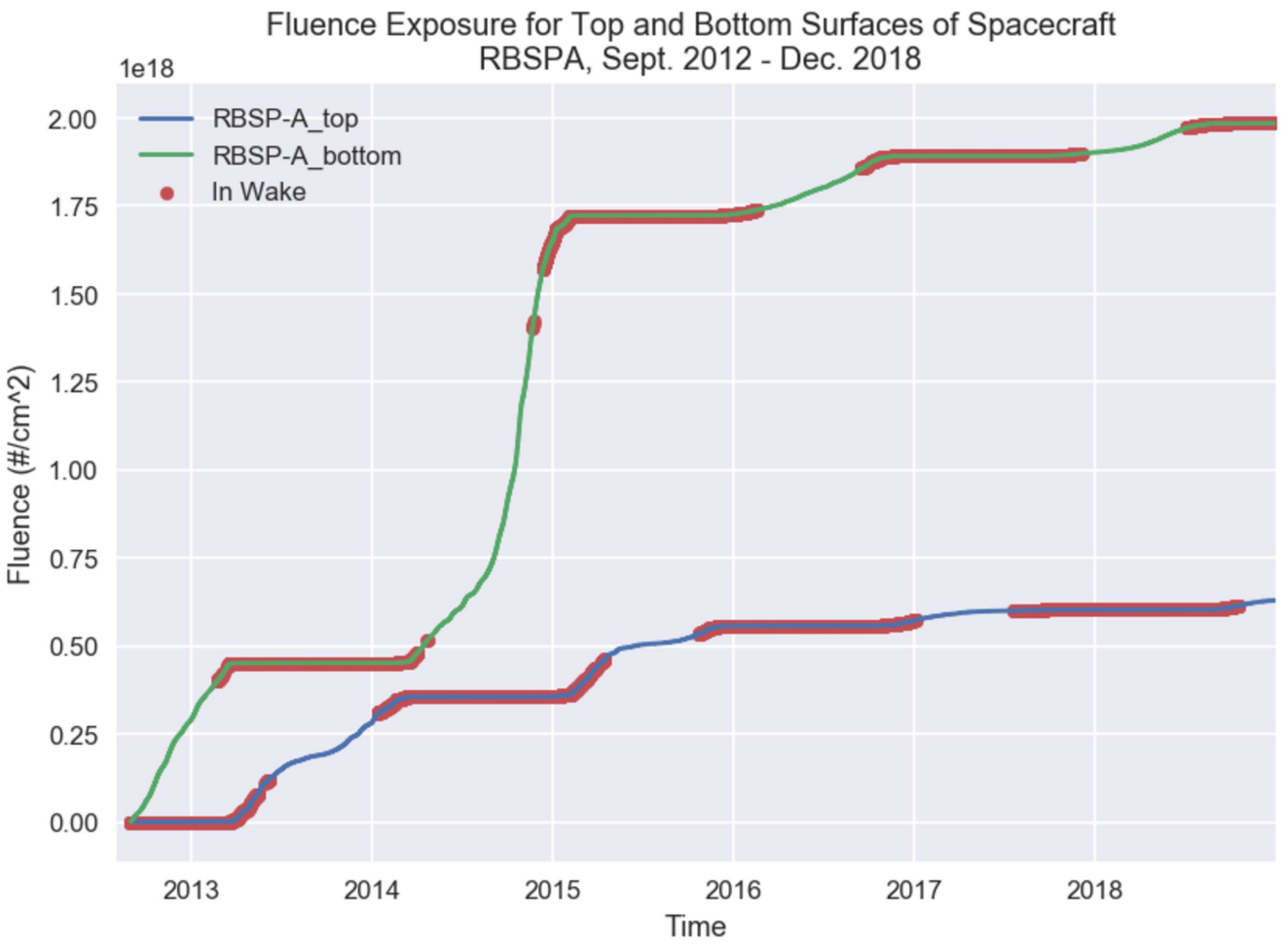
Fluence Exposure for Top and Bottom Surfaces of Spacecraft
RBSPA, Sept. 2012 - Dec. 2018
1e18
RBSP-A_top
RBSP-A_bottom
In Wake
2.00
1.75
1.50
1.25
1.00
0.75
0.50
0.25
0.00
Fluence (#/cm^2)
2013
2014
2015
2016
2017
2018
Time